TDP-43 dysfunction leads to impaired proteostasis and predisposes mice to worse neurological outcomes after brain injury

Melissa S. Rotunno [1,2], Megan Fowler-Magaw [1,3,#], Jianjun Zhong [1,4,#], Kennedy O'Hara [1,3], Elenore A. Wiggin [1,5], Debra Cameron [1], Karly Stallworth [1,2], James Bouley [1], Holly McEachern [6,7], Mina Anadolu [8], Jeffrey A. Nickerson [9], Andrew R. Tapper [10], Susanna Molas [10], Francesca Massi [2,11], Nils Henninger [1,3,12], Oliver D. King [1,3], Daryl A. Bosco [1,2,3,5,11,13*]

[1]Department of Neurology, University of Massachusetts Chan Medical School, Worcester, Massachusetts, MA, 01605

[2]Department of Biochemistry and Molecular Biotechnology, University of Massachusetts Chan Medical School, Worcester, MA, 01605

[3]Neuroscience Program, Morningside Graduate School of Biomedical Sciences, University of Massachusetts Chan Medical School, Worcester, MA, 01605

[4]Department of Neurosurgery, The First Affiliated Hospital of Chongqing Medical University, Chongqing, China, 400016.

[5]Interdisciplinary Graduate Program, Morningside Graduate School of Biomedical Sciences, University of Massachusetts Chan Medical School, Worcester, MA, 01605

[6]RNA Therapeutics Institute, UMass Chan Medical School, Worcester, MA, 01605

[7]RNA Therapeutics and Biology Program, Morningside Graduate School of Biomedical Sciences, University of Massachusetts Chan Medical School, Worcester, MA, 01605

[8]Program in Molecular Medicine, University of Massachusetts Chan Medical School, Worcester, MA, 01605

[9]Department of Pediatrics, University of Massachusetts Medical School, Worcester, Worcester, MA, 01605

25 [10]Department of Neurobiology, Brudnick Neuropsychiatric Research Institute, University of
26 Massachusetts Chan Medical School, Worcester, MA, 01605
27 [11]Biochemistry and Molecular Biotechnology Program, Morningside Graduate School of
28 Biomedical Sciences, University of Massachusetts Chan Medical School, Worcester, MA, 01605
29 [12]Department of Psychiatry, University of Massachusetts Chan Medical School, Worcester, MA
30 [13]Lead Contact
31 [#]These authors contributed equally
32 *To whom correspondence should be addressed: Daryl A. Bosco: Department of Neurology,
33 University of Massachusetts Chan Medical School, Worcester, MA 01605;
34 Daryl.Bosco@umassmed.edu; Tel. (774) 455-3745; Fax. (508) 856-6750
35

36 **ABSTRACT**

37 **Background:** Pathological TAR DNA-binding protein 43 (TDP-43) dysfunction is associated with
38 multiple neurodegenerative disorders. However, the mechanistic link between TDP-43
39 dysfunction and neurodegeneration is poorly understood and likely involves a combination of
40 genetic and environmental risk factors. A major risk factor for neurodegenerative disease is
41 exposure to traumatic brain injury (TBI). Here, we investigated the synergistic interplay between
42 TDP-43 dysfunction and TBI in a murine model of amyotrophic lateral sclerosis (ALS)/
43 frontotemporal dementia (FTD).

44 **Methods:** A model of TDP-43 dysfunction caused by a knock-in Q331K mutation in *Tardbp* was
45 combined with a mild model of TBI. Control conditions included both WT mice and mice with sham
46 surgery. Animals were evaluated for behavioral deficits at timepoints pre- and post-surgery.
47 Additionally, post-mortem brain tissues were examined using RNA sequencing and mass
48 spectrometry-based quantitative proteomics together with histological and biochemical analyses.

Results: Expression of dysfunctional TDP-43 *in vivo* caused deficits in multiple branches of the proteostasis network, including protein folding, protein synthesis, and protein turnover. Examples include mis-expression of chaperones and genes within the ubiquitin-proteosome pathway in mutant TDP-43 versus WT mice. Further, mutant TDP-43 expression correlated with reduced thermostability of proteins associated with the ribosome and the chaperonin containing TCP-1 complex. In response to TBI, mutant TDP-43 mice exhibited significantly worse neurological outcomes relative to WT animals. Heightened neurological deficits in mutant TDP-43 mice following TBI coincided with a robust upregulation of proteostasis- and stress-related genes at the transcript level. However, this upregulation was not detected at the protein level.

Conclusions: Our data demonstrate that expression of dysfunctional TDP-43 leads to deficits within the proteostasis network in vivo at baseline. Despite an upregulation of proteostasis-related genes at the transcript level in mutant TDP-43 mice after TBI, mutant TDP-43 mice exhibit an impaired response to, and recovery from, brain trauma relative to their WT counterparts. Restoring proteostasis is expected to protect against the detrimental effects of TDP-43 dysfunction, especially under stress conditions that promote neurodegenerative disease.

Keywords: TDP-43, traumatic brain injury, proteostasis, ribosome, Proteome Integral Solubility Alteration (PISA), multistep hypothesis, amyotrophic lateral sclerosis, frontotemporal dementia, mass spectrometry, transcriptomics.

BACKGROUND

TAR DNA-binding protein 43 (TDP-43) is an essential RNA/DNA-binding protein that performs critical functions in the context of RNA splicing, transport, and expression.(1) TDP-43 shuttles between the nucleus and cytoplasm while fulfilling these functions, although the protein is predominately expressed in the nucleus under physiological conditions. A significant cytoplasmic shift in TDP-43 localization has been observed in cultured cells exposed to various external stimuli

73 or “stressors” that inhibit proteasomal and transcriptional activity, or that induce hyperosmolarity,
74 hyperexcitability or excitotoxicity.(2-6) While the mechanisms underlying stress-induced
75 cytoplasmic accumulation of TDP-43 have not been fully elucidated, recent reports have shown
76 that both RNA binding capacity and post-translational modification of TDP-43 affect TDP-43
77 subcellular localization.(3, 7-10) TDP-43 has also been identified as a component of cytoplasmic
78 condensates called stress granules, which form in response to acute cellular stress.(11-13)
79 Autosomal dominant mutations in TDP-43 that cause familial amyotrophic lateral sclerosis (ALS)
80 alter the properties of stress granules as well as other TDP-43-associated ribonucleoprotein
81 (RNP) granules,(10-12, 14-16) possibly through altered phase separation behavior of mutant
82 TDP-43 with itself, other RNA-binding proteins and/or RNA.(10, 17-20) Collectively, these
83 observations indicate that subcellular TDP-43 localization can serve as a proxy for cellular stress.
84 Further, the effects of TDP-43 on stress response pathways can be perturbed by disease-causing
85 mutations.
86
87 In addition to TDP-43 mutations in familial ALS, TDP-43 has emerged as a hallmark pathological
88 feature across multiple neurodegenerative disorders termed TDP-43 proteinopathies,(21)
89 including ALS, frontotemporal lobar degeneration (FTLD),(22, 23) Alzheimer’s disease (AD),(24)
90 limbic-predominant age-related TDP-43 encephalopathy (LATE)(25) and chronic traumatic
91 encephalopathy (CTE).(26). Cells with cytoplasmic accumulation and/or nuclear depletion of
92 TDP-43 have been shown to exhibit splicing defects that are consistent with TDP-43 loss-of-
93 function in human post-mortem CNS tissues from ALS/FTLD and AD cases.(4, 27-31) Most cases
94 of human TDP-43 proteinopathy occur sporadically with poorly defined etiologies, and likely
95 develop through a combination of genetic susceptibility and environmental risk factors.(32, 33)
96 Indeed, emerging evidence supports that ALS pathogenesis occurs through a multistep process,
97 even in cases with penetrant genetic mutations in *TARDBP* encoding TDP-43.(34) The multistep
98 hypothesis purports that individual ALS-linked mutations cannot fully account for the disease

99 process, which must include other factors such as additional genetic mutations, environmental
100 exposures and/or physical stress.(34, 35)

101 Traumatic brain injury (TBI) is a form of physical stress that also represents a major risk factor for
102 developing neurodegenerative diseases, including those with TDP-43 pathology.(36) Cytoplasmic
103 shifts in TDP-43 localization have been reported in laboratory animal models of TBI.(13, 37-41)
104 Further, recurrent TBI leads to CTE with cytoplasmic TDP-43 pathology in humans.(26, 42) Here,
105 we sought to investigate the relationship between stress and TDP-43 dysfunction in the context
106 of a multistep model of neurodegenerative disease. To this end, we combined a murine model of
107 TDP-43 dysfunction caused by a genetic knock-in mutation in *Tardbp* together with a mild model
108 of TBI.(43, 44) Our results revealed that mutant TDP-43 mice exhibit significantly worse
109 neurological outcomes during the acute phase post-TBI relative to their wild-type (WT)
110 counterparts. Corresponding transcriptomics and RT-PCR analyses revealed synergistic effects
111 of TDP-43 mutation and TBI on gene expression and processing. For example, a significant
112 upregulation of proteostasis- and stress-related genes was detected specifically in brain tissue
113 from mutant TDP-43 mice after TBI. Many of the pathways that became upregulated in mutant
114 TDP-43 mice following TBI were also highlighted in a recent transcriptomics analysis of post-
115 mortem ALS CNS tissue.(45) While this TBI model caused a cytoplasmic shift in TDP-43
116 localization, this change in TDP-43 localization did not appear to correlate with mis-splicing events
117 caused by TDP-43 loss-of-function. Rather, we found that mutant TDP-43 expression correlated
118 with reduced thermostability of cytoplasmic ribosomal proteins. In fact, diminished thermostability
119 of ribosomal proteins correlated with mutant TDP-43 expression, irrespective of whether mutant
120 TDP-43 mice had been exposed to brain trauma or not. Notably, TDP-43 has been shown to
121 associate with ribosomes and to modulate both global and local translation.(46-49)

122 The outcomes of this study are consistent with a model in which expression of mutant TDP-43
123 leads to deficits throughout the proteostasis network. Upon CNS challenge, compensatory

124 mechanisms appear to become activated in mutant TDP-43 mice, yet these mice fail to mount
125 the physiological response to brain injury exhibited by their WT counterparts. Therefore, our data
126 demonstrate that expression of dysfunctional TDP-43 leads to impaired response to, and recovery
127 from, brain trauma and provide mechanistic insight into TBI as a risk factor for TDP-43
128 proteinopathies. Restoring proteostasis may therefore protect against the effects of TDP-43
129 dysfunction, especially under conditions of CNS challenge that promote neurodegenerative
130 disease.

131 **METHODS**

132 **Animals**

133 All animal related protocols were conducted in accordance with the Guide for the Care and Use
134 of Laboratory Animals published by the National Research Council (US) Committee. The
135 protocols were approved by the Institutional Animal Care and Use Committee (IACUC) of the
136 University of Massachusetts Chan Medical School. Mice with the human-equivalent TDP-43
137 Q331K mutation on a pure C57BL/6J (WT) background were generated and characterized in a
138 previous study.(44) All experiments herein were performed with aged-matched, male mice with
139 either the homozygous TDP-43 Q331K or TDP-43 WT genotype. Mice were generated using
140 standard breeding approaches or via *in vitro* fertilization at the UMass Chan Medical School
141 Transgenic Animal Modeling Core (TAMC; Worcester, MA). All mice were maintained under
142 standard conditions with no more than 5 mice per cage, on a standard 12h light/dark cycle (white
143 light ON at 7:00am and OFF at 7pm), and were provided *ad libitum* access to food and water.

144 **Traumatic brain injury (TBI) surgery**

145 Mice at 16-weeks of age were exposed to TBI or sham surgery. TBI surgeries were based on a
146 previously published protocol.(43) Details of the TBI surgery used herein were published by us
147 elsewhere.(50) Briefly, mice were anesthetized with 3% isoflurane (Pivetal, NDC 46066-755-03)
148 in carrier gas at 1.5 L/min flow. Prior to surgery, buprenorphine (PAR Pharmaceutical, NDC

149 42023-179-05) was administered subcutaneously at 1 mg/kg. Hair was removed from the top of
150 the head and the scalp skin was disinfected with 75% ethanol and betadine. A ~1.2-1.5 cm
151 incision was made along the midline starting approximately 3 mm posterior from the eyes to
152 expose the right parietal skull. The skin over the left and right hemispheres of the skull was
153 excised. The periosteum was removed and the exposed skull was positioned on a cushion
154 beneath the weight-drop. A transducer rod tip was aligned to the skull-top location: 2.5 mm
155 posterior to Bregma and 2 mm lateral to the midline. From a height of 15 cm, a 50-gram
156 weight was released that came into contact with a transducer, which in turn delivered an impact
157 onto the mouse's intact skull (see diagram in **Fig. 1A**). After the impact, mice were placed onto a
158 heating blanket in a supine position for the time needed to wake from the anesthesia (i.e., time
159 required to right themselves to a prone position), which took on the order of minutes for each
160 mouse. Mice were then returned to the anesthesia chamber in preparation for a subsequent
161 impact; this process was repeated a total of ten times within a single surgical session. As the
162 impacts were delivered within the same surgical session and not spaced by days or weeks, this
163 model is not considered a repetitive TBI model that we described previously.(40, 51) After the
164 surgery was completed, cefazolin (HIKMA Pharmaceutical, NDC 0143-9924-90) was
165 administered intramuscularly at 500 mg/kg and meloxicam (Norbrook, NDC 55529-040-10) was
166 administered subcutaneously at 5 mg/kg. Mice were placed on a heating blanket and monitored
167 until they were ambulatory (approximately 15 minutes), and then transferred to their home cage.
168 Buprenorphine was administered as described above at 8 h, 16 h and 24 h after the first dose.
169 For the sham surgery, mice underwent the same procedure as the TBI mice but without the
170 weight-drop impact.

171 **Neurological Severity Score (NSS) Test**

172 The NSS test was performed at 12 time points: pre-surgery and 2h, 24h, 48h, 1 week, 2 weeks,
173 3 weeks, 4 weeks, 8 weeks, 12 weeks, 16 weeks and 20 weeks post-surgery, as previously

174 described in detail.(43, 52) Body weight was measured prior to every NSS testing session. Briefly,
175 the NSS consists of 10 individual tasks designed to assess motor function, alertness and
176 physiological behavior. Each task was completed regardless of whether the mouse passed or
177 failed previous tasks. For each task, mice were assigned a score of 1 to indicate failure of the
178 task or 0 if the task was completed, resulting scores ranging between 0 (no deficit) and 10
179 (maximum deficit). The NSS test was performed by a lab technician who was blinded to the
180 genotype and surgery type of the mice. For statistical analyses, between-group comparisons of
181 the NSS over repeated measurements (time) were conducted using longitudinal mixed models.
182 Time was treated as a categorical variable. The models included group (each group representing
183 both a genotype and surgery type) and time as fixed covariates, as well as the two-way interaction.
184 When the main effects were significant, pairwise comparisons were conducted to identify
185 significance by group and time point. A two-sided $p<0.05$ was considered statistically significant.
186 Statistical analyses were performed using SPSS Statistics Version 29 (IBM-Armonk, NY).

187 **Cued and Contextual Fear Conditioning (CCFC) Test**

188 Animals were generated through two in vitro fertilization procedures at the Transgenic Animal
189 Modeling Core (TAMC) at UMass Chan Medical School using heterozygous Q331K male and
190 female mice. Homozygous Q331K and WT mice were randomly assigned to group 1 or group 2,
191 and both groups were subjected to the CCFC test before surgery. The CCFC test was conducted
192 at the UMass Chan Mouse Behavioral Core facility using the EthoVision XT system (Noldus,
193 BOM-EV-0001). Mice were placed in a Ugo Basile Fear Conditioning Chamber (Noldus, BOM-
194 XUGO-F101) made of optical transparent plastic 26 cm long, 26 cm wide and 38 cm tall. The top
195 of the chamber was equipped with a monochrome GigE camera (Noldus, BOM-XCAM-GIGE)
196 used to track animal movement in real-time during the testing session. The bottom of the chamber
197 contained electricity-conductive metal strips to deliver foot shocks. The chamber was nested in a
198 cabinet equipped with a speaker to deliver white noise and high-frequency tones per the

experimental design detailed below. The cabinet wall was insulated to reduce environmental noise and a built-in ventilator allowed for air-exchange. All the inputs, including white noise, tone, and foot shock, were controlled with a computer-based operation console (Ugo Basile, version 1.1.8.9). EthoVision XT 15 software was used for animal tracking and data analysis. The live tracking started immediately when the animal entered the chamber, after which there was a 60s delay prior to the start of an input. The full test session was conducted over four consecutive days as follows. Note that the white noise and the tone input were delivered randomly, with random intervals (ranging from 5s to 30s) between these two inputs for all tests on each day.

Day 1:

White noise: 50% intensity, 30s duration, and repeated 5 times.

Tone: 1000 Hz, 50% intensity, 30s duration, and repeated 5 times.

Day 2:

White noise: 50% intensity, 30s duration, and repeated 5 times.

Tone: 1000 Hz, 50% intensity, 30s duration, and repeated 5 times.

Electrical foot shock: 0.75 mA intensity that occurred at the last second of each tone. Each mouse received five foot shocks in total on Day 2 with each shock lasting for 1s.

Day 3:

White noise: 50% intensity, 30s duration, and repeated 5 times.

Tone: 1000 Hz, 50% intensity, 30s duration, and repeated 5 times.

Novel context: To create a novel context, a new scent and visual component were introduced to the chamber as follows. One drop of vanilla extract (novel scent) was applied to a piece of tissue paper, which was placed in the feces tray underneath the chamber. Paper boards with white and black stripes (novel visual) were attached to the outer side of the chamber.

Day 4:

The context was reverted as per Days 1 and 2 (i.e., the paper boards were removed and the feces tray cleaned before Day 4) for testing on Day 4.

225 Neither white noise nor tone were implemented.

226 Below is a table summarizing the inputs and contexts for the CCFC test:

	Day 1	Day 2	Day 3	Day 4
White noise	+	+	+	-
Tone	+	+	+	-
Foot shock	-	+	-	-
Novel context	-	-	+	-

227 For analysis of Days 1-3, the initial 29s of each input was extracted to avoid potential interference
228 from the last second when the foot shock was delivered. Therefore, the total duration for white
229 noise and tone inputs is 29s x 5 = 145s. For Day 4, the consecutive 145s after the initial 60s delay
230 was extracted for the analysis. Mouse movement was detected by the software at the pixel level
231 for the entire chamber from one video frame to the next. Thresholds based on animal activity
232 within the chamber were set as follows: immobility state (<0.1% pixel change in the chamber),
233 movement between immobility and walking (between 0.1% and 0.5%) and walking (>0.5%). The
234 amount of time animals spent in an immobility state was interpreted as freezing behavior and
235 plotted for each day (Day 1-4). The statistical analysis was performed as described above for
236 NSS, where between-group comparisons over repeated measurements (time) were conducted
237 using longitudinal mixed models. Time was treated as a categorical variable. The models included
238 group and time as fixed covariates, as well as the two-way interaction. When the main effects
239 were significant, pairwise comparisons were conducted to identify significance by group and time
240 point. A two-sided $p<0.05$ was considered statistically significant. Statistical analyses were
241 performed using SPSS Statistics Version 29 (IBM-Armonk, NY).

242 **RNA isolation**

243 Mouse brain tissue samples (~40 mg and 4 mm of diameter) were collected from the impact site
244 (**Fig. 1A**) and the corresponding site on the contralateral side using a sterile disposable biopsy

245 punch (Integra Miltex, 33-32) that excised tissue from the brain surface (i.e., cortex) to the brain
246 bottom (i.e., hypothalamus). Total RNA was isolated from mouse brain tissues using Qiagen's
247 RNeasy Lipid Tissue Mini Kit (Cat. No. 74804) with DNase treatment following the manufacturer's
248 protocols. RNA concentration and absorbance were measured by a Nanodrop device (ND1000).
249 Samples with A260/A280 between 1.8 to 2.2 were considered suitable for downstream
250 applications.
251
252 **Transcriptome analysis by RNA-sequencing (RNAseq)**
253 For the 24h-post TBI timepoint, RNAseq analysis was performed on RNA isolated from brain
254 tissue as described above for six groups of mice: homozygous Q331K and WT genotypes, each
255 under naïve, sham, and TBI conditions. For the 7mo-post TBI timepoint, only sham and TBI
256 conditions for homozygous Q331K and WT genotypes were included. Sham and TBI conditions
257 are described under TBI surgery. Naïve mice were not subjected to surgery and are therefore
258 treated a separate control group than sham surgery mice. Between 3-6 mice were included per
259 group for a total of 46 samples. RNA quality assessment, library preparation and sequencing were
260 conducted by Novogene Co., LTD (Beijing, China). Poly-T oligo-attached magnetic beads were
261 used for poly-A capture, random hexamer primers for first strand cDNA synthesis, and dTTP for
262 second strand cDNA synthesis of non-directional libraries. Libraries were sequenced to a depth
263 of 50M-125M raw read pairs (2x150 PE) per sample using an Illumina NovaSeq 6000 sequencer.
264 After trimming adapter sequences and low-quality bases, reads were mapped with HISAT2
265 (2.0.5)(53) to the mouse mm39 reference genome with Ensembl release 107 gene annotations.
266 Two samples (one Q331K sham and one Q331K TBI) from the 24h post-TBI timepoint were
267 excluded from further analyses, as they were strong outliers in Principle Component Analysis
268 (PCA) of expression values (counts-per-million on $\log_2$ scale with prior.count=1; **Fig. S1A**); see
269 **Additional File 1** for all supplemental figures. These samples were also outliers for several
270 mapping quality control (QC) metrics, with higher-than-usual fractions of multi-mapping, exonic,

271 and unspliced reads. Two samples (one Q331K sham and one WT TBI) were also excluded from
272 the 7mo-post TBI dataset because they were determined to by outliers in the PCA analysis (**Fig.**
273 **S1B**).
274
275 Differential gene expression analyses were performed in R (4.3.2) using quasi-likelihood methods
276 in the edgeR package (4.0.12).(54) Data from 24hr-post TBI and 7mo-post TBI experiments were
277 analyzed separately. The TMM method was used for computing normalized library sizes and
278 genes with low counts were filtered out in preprocessing. For both datasets, ~25,000 genes were
279 retained with at least 5 scaled counts in at least 3 samples, where the scaling adjusts for
280 differences in total library sizes (read counts across all genes) between samples while keeping
281 the median library size unchanged. The function glmQLFit (with non-default options robust=T
282 and prior.count=1) was used to fit the expression data with a design matrix that included factors
283 for injury (INJ, with levels Naïve, Sham, and TBI), genotype (GT, with levels Q331K and WT) and
284 their interaction (model formula ~0 + GT:INJ). For the 7mo-post TBI data the model also included
285 an additive factor for IVF batch (with two levels, 162 and 167). Differential expression was
286 assessed using the function glmQLFTest for contrasts that included nine simple between-group
287 comparisons (WT.TBI vs WT.Sham, etc.); contrasts for main effects of GT (Q331K vs WT) and
288 INJ (TBI vs Sham), though in both cases excluding the groups with INJ=Naïve; and a test for an
289 interaction between GT and INJ, again excluding the groups with INJ=Naïve. Supplemental Table
290 I includes the $\log_2$(fold-change) [LFC], p-value, and FDR for each gene for each contrast.
291
292 Gene Set Enrichment Analysis (GSEA, 4.3.3) was performed using the Hallmark
293 (mh.all.v2024.1.Mm.symbols.gmt) and Gene Ontology Biological Process (GOBP,
294 m5.go.bp.v2024.1.Mm.symbols.gmt) gene set collections from the Molecular Signatures
295 Database (MSigDB).(55-59) Cutoffs on Normalized Enrichment Score (NES) and adjusted p-
296 value (FDR) were used to determine significantly altered gene sets (|NES| > 1.5 and FDR<0.05).

297 NES is a score that reflects the overrepresentation of a gene set at the upper (positive value) or
298 lower (negative value) end of a ranked gene list, after normalization to account for variation in
299 gene set size. The gene list was pre-ranked based on directional p-values for the indicated
300 comparison (-log(p-value)*sign of log_2(fold change)). A weighted enrichment statistic was used in
301 the analysis. The 10 top gene sets based on highest |NES| are displayed for all enrichment
302 analyses. If fewer then 10 are displayed then all gene sets that meet the cutoff criteria are shown.
303 All gene set hits that meet the cutoff criteria can be found in **Supplemental Table II**.
304

305 **Quantitative Proteomics**

306 Mice were perfused with PBS prior to tissue isolation for all proteomic analyses. Mouse brain
307 tissue samples were collected as described above under RNA isolation and cut into ~1 mm
308 diameter pieces. For whole brain proteomics, the tissue was transferred to a pre-cooled glass
309 homogenizer on ice with 900 µl of RIPA buffer (Sigma-Aldrich R0278-50ML) containing 1x
310 protease inhibitor (Roche, 11873580001) and 1x phosphatase inhibitor (Roche, 04906837001).
311 Complete tissue homogenization was performed with a WHEATON Power Homogenizer and
312 Overhead Stirrer (catalog number 903475, serial number G082210) by setting the stirring speed
313 on level 2 for 1 minute. The sample was transferred to a plastic tube together with 300ul of RIPA
314 buffer that was added to rinse the homogenizer. The sample was left on ice for 30 min and then
315 centrifuged at 15,899 xg for 10 min at 4°C in a table-top centrifuge (AXYGEN, serial number
316 LRMPL1-1710018, lot number 04619100). The supernatant was transferred into a fresh tube and
317 the bicinchoninic acid (BCA) assay (Thermo Scientific, 23223) was used to measure the protein
318 concentration. For cytoplasmic samples depleted of nuclei and mitochondria for PISA (below),
319 samples were homogenized in 1.1 mL of KPBS (130 mM KCl, 10 mM KH_2PO_4, pH 7.3). Minced
320 tissue was homogenized twice on level 2 for 1 min each with 1 min on ice in between.
321 Homogenate was transferred to a 1.5 ml Eppendorf tube. The glass tube was rinsed with 0.3 ml
322 of KPBS +PI and added to a 1.5 ml Eppendorf tube. Samples were spun twice at 600 xg at 4°C

323 for 5 min with supernatant moved to a fresh Eppendorf tube each time to remove the nuclear
324 fraction and debris. Samples were then centrifuged at 7,000 xg at 4°C for 10 min to remove
325 mitochondria.

326 For PISA analysis, cytoplasmic samples depleted of nuclei and mitochondria were diluted in half
327 to 1 mg/ml with PISA lysis buffer (2 mM MgCl2, 1% CA630, PBS (Corning 21-031-CV)). Lysates
328 were incubated on ice for 30 min and subdivided into 4 aliquots in PCR strip tubes. One aliquot
329 was kept on ice to use for the total protein level quantitative proteomics. The remaining three
330 aliquots were exposed to a single temperature (52°C, 53°C, 54°C) for 3 min followed by
331 equilibration to 25°C for 5 min. The three temperatures (52°C, 53°C, 54°C) for each sample were
332 combined and centrifuged at 20,817 xg for 99 min at 4°C to remove aggregated protein.
333 Supernatant (soluble fraction) was moved to a new tube. All samples were frozen on dry ice and
334 dried down in speedvac (**Fig. S10A**).

335 For tandem mass tag (TMT) proteomics, 50 μg of protein (whole brain) or 12 μg (organelle
336 depleted cytoplasm) was dried down in a speedvac (Thermo Scientific, SPD111V), resuspended
337 in 23 μl of 1x lysis buffer (5% SDS, 50 mM TEAB, pH8.5) and digested with Trypsin/LysC (Thermo
338 Scientific, A41007) using S-Trap micro columns (ProtiFi, C02-micro-80) as described by the
339 manufacturer. Eluted peptides were dried in a speedvac and resuspended in 20 μl (whole brain)
340 or 5 μl (organelle depleted cytoplasm) of 100 mM TEAB pH 8.5. The resuspended peptides were
341 added to a tube containing TMT tag for a final protein:TMT ratio of 1:2 (ThermoFisher, #A44521).
342 The reaction was quenched with 0.5 μl of 5% hydroxylamine and incubated for 15 min at 25°C
343 with shaking (300 rpm). Quenched samples were combined and dried down in aliquots with 50
344 μg set aside as "pre-fractionation" sample. For fractionation (whole brain only), 125 μg aliquot
345 was resuspended in 300 μl of 0.1% TFA and sonicated for 5 min. The sample was subjected to a
346 high pH reversed phase fractionation procedure as described by manufacturer (Pierce,

347 #84868). Fractions 2 and 8 were combined and dried down. Fractions 3-7 were kept separate
348 and dried down. Fractions and input samples were reconstituted with 20 μl of 5% acetonitrile,
349 0.1% formic acid and 3.8 μl was injected per replicate.

350 Liquid chromatography tandem mass spectrometry (LC–MS/MS) experiments were performed in
351 duplicate for fractionated samples and in triplicate for unfractionated samples. Samples were run
352 in a 145 min gradient from 10% of acetonitrile (0.1% formic acid) to 70% acetonitrile, 0.1% formic
353 acid in data dependent mode on a nanoACQUITY UltraPerformance LC (UPLC; Waters, Milford,
354 MA, USA) coupled to an Orbitrap Fusion Lumos Tribid mass spectrometer. MS data acquisition
355 was collected from 400 to 1400 m/z with a resolution of 120,000. MS2 Data Dependent Acquisition
356 was acquired with a resolution of 50000 at m/z 200 with a mass injection time of 120 ms. Other
357 acquisition methods and column setup were identical to those described previously.(60) Raw
358 data files were processed with MaxQuant version 2.4.11.0. with reviewed entries only of mouse
359 uniprotKB FASTA file (downloaded 08/09/2023) to identify peptide-spectrum matches (PSM) and
360 to consolidate replicate injections.(61) Search parameters included Trypsin/P enzyme, fixed
361 modification of carbamidomethylation on cysteine (+57 on C) and variable modifications of
362 oxidized methionine (+16 on M), phosphorylation of serine (S), threonine (T), and tyrosine (Y)
363 (+80 on STY) and N-terminal acetylation (+42). The files were processed with Reporter MS2 type
364 set to TMT 16-plex (+304 on peptide N-Terminal and Lysine). Assignments were made using a
365 20-ppm mass tolerance for first search and 4.5 for main search for the precursor and 0.5 Da mass
366 tolerance for the fragments with a 1% FDR set for PSM and Protein. The proteinGroups output
367 text file was imported into Perseus (2.0.10.0) for $\log_2$ transformation, imputation using values
368 based on normal distribution, and quantile normalization.(62) Additional filters included numerical
369 value in at least 4 of the 16 samples and 2 unique peptides for protein identification. The exported
370 table was then processed in RStudio (R version 4.3.3) using a linear model in limma (3.58.1) and
371 empirical Bayes test for statistics. Contrasts included four between-group comparisons (WT.TBI

372 vs WT.Sham, Q331K.TBI vs Q331K.Sham, WT.TBI vs Q331K.TBI, and WT.Sham vs
373 Q331K.Sham), contrasts for main effects of GT (Q331K vs WT) and INJ (TBI vs Sham). Proteins
374 with an FDR < 0.1 were considered significantly different between groups. For the PISA data
375 processing, one Q331K sham sample was identified as an outlier based on total intensity and
376 excluded from further analyses. Data are available via ProteomeXchange with
377 identifier PXD068825 and 10.6019/PXD068825.

378 **Western blotting**

379 For Western blot analyses, protein samples were mixed with loading buffer (Boston BioProducts,
380 BP-111R) and boiled at 100 °C for 5 min. Gel electrophoresis was performed with the BIO-RAD
381 PowerPac™ HC followed by a transfer onto polyvinylidene fluoride (PVDF; Merck Millipore,
382 IPFL00010) membrane. The PVDF membrane was blocked for 1h at ambient temperature using
383 Intercept Blocking Buffer (LI-COR, 927-70003) and then primary antibody (see table below) was
384 incubated at 4°C overnight (>12 h) in PBST and secondary antibody was incubated at ambient
385 temperature for 1 h in blocking buffer. The PVDF membrane was imaged using the LI-COR
386 ODYSSEY infrared imager system (Serial No. ODY-2215). The target protein intensity was
387 quantified using Image Studio software (Lite Ver 5.2).

Antibody	Manufacturer	Catalog #	Dilution
H3	Proteintech	17168-1-AP	1:1000
Calr	Enzo life sciences	ADI-SPA-602	1:1000
Cox4	Abcam	AB14744-1005	1:1500
GAPDH	Sigma-Aldrich	G8795	1:2000
Rpl4	Proteintech	11302-1-AP	1:2000
Rps6	Cell Signaling	2217	1:500
TDP43	Encor	MCA3H8	1:5000
Anti-Mouse IgG 680	LICORbio	926-68072	1:10,000
Anti-Rabbit IgG 800	LICORbio	926-32211	1:10,000

388

389 **Immunostaining**

390 Mice were euthanized and transcardially perfused with PBS and 4% paraformaldehyde (PFA;
391 Fisher Scientific, AAA1131336) in 1X PBS, pH 7.4. Mice were decapitated, and the scalp and

392 skull carefully removed to harvest the intact brain. All brain samples were immersed in 4% PFA
393 solution for 24h at 4°C for post-fixation. A brain matrix (CellPoint Scientific, Alto Acrylic 1mm
394 Mouse Brain Coronal) was used to pre-section the brains into anterior, medial, posterior and
395 cerebellar sections, which were embedded in paraffin by the Morphology Core (UMass Chan
396 Medical School). Coronal sections of 7 μm thickness were prepared on a Leica RM2125 RTS and
397 mounted onto charged microscope slides (Globe Scientific Cat#1354W). Prior to immunostaining,
398 tissues were deparaffinized with xylenes (Fisher Scientific, X3P-1GAL) and rehydrated in 100%
399 and 70% ethanol (Fisher Scientific, 04355223EA). Tissues were subjected to antigen retrieval
400 using 10mM Sodium Citrate (Fisher Scientific, S25545) containing 0.05% Tween 20 (Fisher
401 Scientific, BP337-500) at pH 6.0, heated to boiling, and then maintained at 95°C in a steamer
402 (Black&Decker Cat# HS1050) for 30 minutes. Tissues were blocked using 1% bovine serum
403 albumin (BSA; Fisher Scientific, BP1600-100) and 3% horse serum (Gibco, 26050-070) in PBS
404 for 1h at ambient temperature. Tissues were probed with rabbit anti-TDP-43 (1:250 Proteintech,
405 10782-2-AP) and chicken anti-NeuN (Millipore Sigma, ABN91) antibodies at 4°C overnight.
406 Tissues were incubated at ambient temperature for 1h with fluorophore-conjugated secondary
407 antibodies (Jackson ImmunoResearch Laboratories) at 1:500 and counterstained with DAPI.
408 Prolong Gold antifade reagent (Invitrogen, P36930) with a refractive index of 1.46 was used to
409 mount coverslips onto the tissues.
410
411 **Confocal Microscopy**
412 TDP-43/NeuN/DAPI immunofluorescence images were obtained using a Leica TCS SP5II (S/N:
413 5100001537, 11888906 BZ:01) confocal microscope. A 40x objective lens with oil was used to
414 acquire images. Leica Application Suite Advanced Fluorescence (LAS AF) software was used for
415 image acquisition as follows: imaging mode: XYZ; Sequential imaging: on; Format: 512x512;
416 Pinhole: on; Speed: 400 Hz; Line average: 1; Frame average: 3, Accu for Line average: 1; Accu
417 for Frame average: 1; Z-stack mode: Z-wide; Sequential scan mode: between frames, number of

418 steps: 3; Z-step size: ~0.5 µm. Using these settings, images were collected in the following order:
419 ipsilateral cortex, ipsilateral amygdala, ipsilateral hypothalamus, contralateral hypothalamus,
420 contralateral amygdala and contralateral cortex.

421 **TDP-43 localization analyses**

422 TDP-43 nuclear-to-cytoplasmic (N/C) ratio analysis was performed with 40x confocal images
423 described above on a per image basis with a custom macro generated with Fiji (**Additional file**
424 **2).** (63) DAPI signal was used to define the area of nuclear TDP-43 fluorescence and the
425 cytoplasm was defined as any area outside of the DAPI-defined region. Mean TDP-43
426 fluorescence intensity was measured for the nuclear and cytoplasmic regions, and the N/C ratio
427 was calculated by dividing the mean nuclear TDP-43 signal by the mean cytoplasmic TDP-43
428 signal.

429 TDP-43 N/C ratio analysis was also performed on a per-cell basis using a customized pipeline
430 that was developed in CellProfiler(64) for calculation of the percentage of cells with increased
431 cytoplasmic TDP-43 **(Additional file 3)**. DAPI signal was used to identify the nuclear region,
432 which was then expanded by 8 pixels to capture a contiguous cytoplasmic region. The mean TDP-
433 43 fluorescence intensity was measured for the defined nuclear and cytoplasmic regions and the
434 N/C ratio was calculated as described above for the per image analysis. Cells with an N/C ratio
435 <5.72 were classified as having cytoplasmic TDP-43. This threshold was determined using the
436 average N/C ratio of each field of view (FOV) in the WT sham condition (representing a condition
437 that did not exhibit robust cytoplasmic TDP-43) minus one standard deviation. Within a FOV, the
438 number of cells with an N/C ratio <5.72 was then divided by the total number of cells, multiplied
439 by 100 to obtain the percentage cells with cytoplasmic TDP-43 for each condition.
440

441 The CellProfiler pipeline above was also used to measure the distribution of TDP-43 signal within
442 the nucleus and to quantify the number of cells with a “ring-like” TDP-43 staining appearance.

443 The nucleus, as defined by DAPI, was divided into three concentric regions using the Measure
444 Object Intensity Distribution module in CellProfiler and setting the number of bins to three. The
445 rings are therefore proportional to the size of each nucleus and nuclear area is accounted for in
446 the pipeline. For example, the outer ring represented the outer 1/3 of the nucleus, regardless of
447 nuclear size. TDP-43 fluorescent signal was measured within each of the three nuclear ring-
448 regions. Cells exhibiting ring-like TDP-43 staining were defined as those with >56% of the total
449 nuclear TDP-43 signal in the outer region (i.e., at the boundary of the nuclear envelope). This
450 threshold was determined by calculating the average percent of total nuclear TDP-43 signal
451 present in the outer region of the nucleus (the outermost concentric ring) in all WT sham cells
452 plus one standard deviation. Within a FOV, the percentage of cells with >56% nuclear TDP-43
453 signal in the outer nucleus out of the total cells per each condition was determined and used for
454 analysis.
455
456 The outcomes of the TDP-43 localization analyses above were combined to generate a measure
457 of cells with altered TDP-43 localization, which included cells that exhibited TDP-43 ring-like
458 and/or cytoplasmic TDP-43 according to the following parameters:
459

TDP-43 localization	N/C Ratio Value	% TDP-43 in outer ring of nucleus
Nuclear	>5.72	<56%
Ring-like, no cytoplasmic	>5.72	>56%
Ring-like with cytoplasmic	<5.72	>56%
Cytoplasmic, without ring-like	<5.72	<56%

460
461 The total number of cells that demonstrated each of the four TDP-43 distributions from the above
462 table (nuclear, ring-like +/- cytoplasmic and cytoplasmic) was summed then divided by the total
463 cells per FOV in each condition and multiplied by 100 to calculate the percent of cells with altered

464 TDP-43 localization per mouse. To visualize the overall effect of genotype and TBI on altered
465 TDP-43 localization, the percent of cells with each TDP-43 distribution was averaged across all
466 mice in each condition by FOV and plotted in a stacked bar graph in **Fig. 4**.
467
468 **Reverse transcription polymerase chain reaction (RT-PCR)**
469 RNA was isolated as described above and cDNA was synthesized using iScript Reverse
470 Transcription Supermix (Bio-Rad, 9170-8840) according to the manufacturer's instructions. RT-
471 PCR was performed on mouse tissue using 2x Taq RED Master Mix (APExBio Cat. No. K1034)
472 with the primers listed (**Supp. Table V**) with a touchdown PCR according to the manufacturer's
473 instructions. Products were separated on 3.5% agarose gels using the SYBR Safe DNA gel stain
474 (Invitrogen) and imaging was performed using the Bio-Rad Chemidoc software. Quantification of
475 the different isoforms was performed with ImageStudio software (LICORbio), using manual
476 settings to analyze the densitometry of each band. The intensity ratios between products with
477 included and excluded exons were analyzed for samples from a minimum of four individual mice
478 per group.
479
480 **Structural analysis**
481 The mm39 reference genome in Integrative Genomics Viewer was used to identify exons in
482 *Ube3c*. The splice variant, with the corresponding exon removed from the amino acid sequence,
483 was modeled in AlphaFold 3.(65) Structural alignments of the models were performed in PyMOL
484 (Molecular Graphics System, Version 3.1.3.1, Schrödinger) by minimizing the root-mean-square
485 deviation (RMSD) between superimposed structures. The resulting aligned structures were
486 visualized in PyMOL.
487
488 **Ribosomal Profiling of cytoplasmic fractions**

489 Ribosomal profiling was performed as previously described (66) on cytoplasmic fractions. A 20%
490 to 50% sucrose gradient was prepared using a Gradient Master 107 (BioComp) in 14 x 89 mm
491 polypropylene ultracentrifuge tubes (Beckman 331372). A total of 6 mL of 20% sucrose solution
492 in 10 mM HEPES pH7.4, 150 mM NaCl, 5 mM MgCl2 with 100 μg/ml of cycloheximide, was added
493 and overlayed with 50% sucrose solution made using the same buffer conditions. The top of the
494 sucrose gradient (300 μl) was removed and replaced with 300 μl of sample (800 μg) containing
495 100 μg/ml of cycloheximide and 40 U/ml of RNaseIN. Samples were centrifuged at 197,000 x g
496 for 2h at 4°C using a Beckman SW41 Ti rotor. Samples were loaded on a Density Gradient
497 Fractionation system (Brandel), pushed with 60% sucrose and 0.72 ml fractions were collected
498 with real-time UV monitoring at 254 nm using an ISCO UA-6 UV detector. Protein was precipitated
499 from fractions using cold acetone. Protein pellets were collected by centrifugation at 13,000 x g
500 for 10 min at 4°C, resuspend in 100 μl of SDS loading buffer, and heated for 5 min at 90°C.
501

502 **RESULTS**

503 **Mutant TDP-43 mice exhibit heightened neurological deficits and delayed recovery**
504 **following TBI.** To examine the effects of TDP-43 dysfunction in the context of CNS challenge,
505 we administered a mild TBI using a weight-drop device (**Fig. 1A**) to mice harboring a knock-in
506 ALS-linked Q331K mutation in TDP-43.(44) TDP-43 Q331K mice (hereon referred to as Q331K
507 mice) exhibit phenotypes consistent with frontotemporal dementia (FTD), but without motor
508 deficits or motor neuron degeneration that is associated with ALS.(44) This mild TBI model has
509 been described by us previously.(39, 40, 43, 50, 51, 67) Here, a free-falling 50g weight was
510 dropped from a height of 15cm and used to deliver multiple impacts to the mouse's exposed but
511 intact skull within a single surgical session (**Fig. 1A,B**). Sham animals underwent the same
512 surgery as TBI animals to retract the skin from the skull but without any impact.

513 TBI studies included four main groups of mice at 16-weeks of age: Q331K and WT mice,
514 each with sham or TBI surgery. Neurological evaluations of motor function, alertness and
515 physiological behavior pre- and post-TBI were accomplished using a set of 10 tasks.(52) The
516 results of these tests are reported as a Neurological Severity Score (NSS), which is used to
517 assess potential neurological deficits following TBI in rodent models, where a higher score reflects
518 worse neurological deficits.(52). Consistent with our previous reports,(39, 43, 67) WT mice
519 exhibited worse NSS scores after TBI compared to their sham counterparts at 2 h post-TBI.
520 Notably, Q331K mice exhibited significantly worse NSS scores during the acute phase post-TBI
521 (i.e., 2h, 24h, and 48h post-TBI) compared to their WT counterparts, demonstrating heightened
522 vulnerability and delayed recovery to brain trauma **(Fig. 1C)**. All groups returned to baseline by
523 one-week post-TBI, as expected for a mild-TBI paradigm.(43)

524 Mice were also evaluated for long-term deficits resulting from TBI using the cued and contextual
525 fear conditioning (CCFC) test, an assessment of learning and memory.(68, 69) The CCFC test
526 consisted of four days, with habituation on day 1 (**Fig. 1D**), conditioning with a paired tone and
527 foot shock on day 2 (**Fig. 1E**), testing recall of the foot shock in response to the tone (i.e., cue) on
528 day 3 (**Fig. 1F**), and testing recall of the CCFC chamber (i.e., context) on day 4 (**Fig. 1G**). An
529 animal's freezing behavior on days 3 and 4 reflects its capacity for learning and memory, where
530 attenuated freezing is indicative of deficits in learning and memory.(68, 69) WT and Q331K mice
531 were randomly assigned to group 1 or group 2, and both groups were subjected to the CCFC test
532 before surgery. Group 1 and group 2 animals were then, respectively, administered sham or TBI
533 surgery and assessed using the CCFC test again 5-months post-surgery. Linear mixed effect
534 analyses were then used to determine potential differences between groups and over time (i.e.,
535 between pre- and post-surgery) for the CCFC test. This uncovered significant effects for the

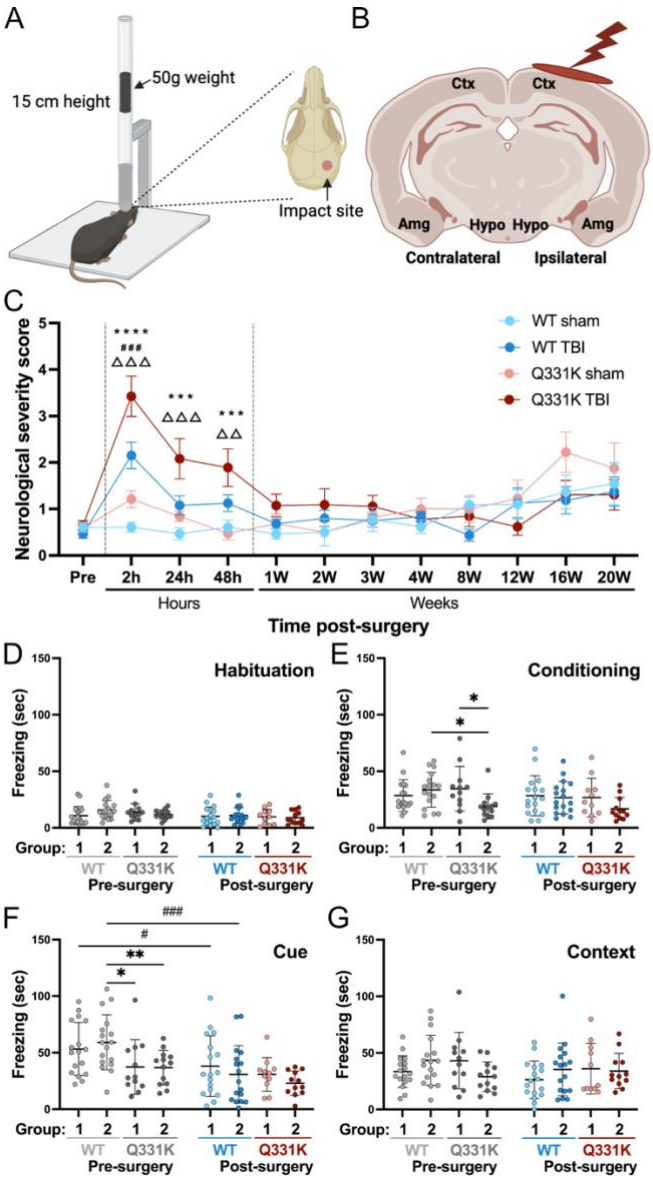

Figure 1. Neurological and cognitive deficits in mice with and without brain trauma. (A) Diagram of the weight drop device used to induce multiple closed-skull impacts with a 50g weight dropped from a 15cm height within a single surgical session. Location of impact site (red circle) is shown on the right. Created with biorender.com. **(B)** Illustration depicting the location of the impact site (red lightning bolt and oval). Several brain regions of interest are highlighted as follows: cortex (Ctx), amygdala (Amg), and hypothalamus (Hypo) on both ipsilateral and contralateral sides of the brain. Created with biorender.com. **(C)** Neurological severity score (NSS) plotted as a function of time post-surgery and cohort (see key). Statistically significant comparisons shown on the graph include Q331K TBI versus Q331K sham at 2h (****$p=2.98e^{-6}$), 24h (***p=0.00058) and 48h (***p=0.00018) post-surgery, WT TBI versus WT sham at 2h post-surgery ($^{\#\#\#}$p=0.00070) and Q331K TBI versus WT TBI at 2h ($^{\Delta\Delta\Delta}$p=0.00026), 24h ($^{\Delta\Delta\Delta}$p=0.00022) and 48h ($^{\Delta\Delta}$p=0.0058) post-surgery. Additional significant comparisons include Q331K TBI versus WT sham at 2h ($p=7.0e^{-10}$), 24h ($p=2.54e^{-6}$) and 48h (p=0.00014) post-surgery. **(D-G)** Mice were randomly assigned to Group 1 (sham) or 2 (TBI). Results of the cued and contextual fear conditioning (CCFC) test. **(E)** The Q331K-2 cohort exhibited altered freezing behavior during conditioning compared to Q331K-1 (*p=0.028) and WT-2 (*p=0.017). **(F)** Both Q331K cohorts exhibited attenuated cue-induced freezing relative to WT animals (*p=0.012 for WT-2 vs. Q331K-1; **p=0.009 for WT-2 vs. Q331K-2) pre-surgery. WT animals exhibited attenuated cue-induced 5-months after sham ($^{\#}$p=0.048) and TBI ($^{\#\#\#}$p<0.001) surgeries.

564 conditioning (Day 2) and cue-induced freezing response (Day 3). For conditioning, significant
565 group (P=0.010; numerator degrees of freedom or df=3, denominator df=107.770, F=3.991)
566 effects were detected, but not significant time (P=0.139; df=1, denominator df=107.773, F=2.220)
567 or group x time interaction (P = 0.724; numerator df=3, denominator df=107.770, F=0.441) effects.
568 On pair-wise testing, one of the Q331K cohorts was found to exhibit altered freezing behavior
569 during conditioning compared to one of the WT cohorts and also to the other Q33K1 cohort (**Fig.**
570 **1E**). As mice were randomly assigned to groups 1 and 2, the reason for the latter difference in
571 pre-surgery mice is unclear. For cue-induced freezing response, significant group (P = 0.016;
572 numerator df=3, denominator df=107.938, F=3.595) and time (P <0.001; numerator df=1,
573 denominator df=107.955, F=14.651) effects were detected, but not significant group x time
574 interaction (P = 0.298; numerator df=3, denominator df=107.938, F=1.243) effects. On pair-wise
575 testing, both Q331K cohorts exhibited attenuated cue-induced freezing on day 3 relative to WT
576 animals, where comparisons with the WT-2 cohort reached significance (**Fig. 1F**). These
577 outcomes are consistent with Q331K mice exhibiting cognitive deficits prior to surgery, as shown
578 for other cognition tests described by White et al.(44)

579 Both WT sham and WT TBI groups showed differences in the cue-induced freezing response at
580 5 months post-surgery versus the pre-surgery timepoint (**Fig. 1F**). The reduced freezing behavior
581 in WT sham animals 5 months post-surgery may stem from aging and/or adverse effects related
582 to the sham surgery. Conversely, Q331K mice showed no difference in the cue-induced freezing
583 response at 5 months when compared to pre-surgery, when they already exhibited cognitive
584 deficits. Therefore, there may be a ceiling effect with respect to cognitive dysfunction in Q331K
585 mice, given that Q331K mice exhibit similar cue-induced freezing behavior pre- and post-surgery,
586 regardless of surgery-type or age (**Fig. 1F**). Finally, there were no significant differences in
587 context-induced fear behavior due to genotype or surgery (**Fig. 1G**). Taken together, this mild-
588 TBI paradigm appears to exert minimal long-term effects on learning and memory, whereas

589 mutant TDP-43 expression may be sufficient to cause deficits in the amygdala, the brain region
590 that influences cue-induced behavior more so than others such as the hippocampus.(68, 69)

591 **Proteostasis-related genes become upregulated in mutant TDP-43 mouse brain after TBI.**
592 To investigate the gene expression changes associated with enhanced neurological severity
593 scores and delayed recovery in Q331K mice (**Fig. 1C**), bulk RNA sequencing (RNAseq) was
594 pursued using mouse whole brain lysate near the impact site (**Fig. 1A**) at the 24h post-TBI
595 timepoint. This analysis focused on four groups: Q331K and WT mice, each with sham or TBI
596 surgery. Of the ~25,000 genes that remained after filtering out genes with very low expression,
597 our analysis identified 228 that were differentially expressed between the Q331K TBI and WT TBI
598 mice (**Fig. 2A, Supp. Table I**).

599 Gene Set Enrichment Analysis(58, 59) was performed using the hallmark and Gene Ontology
600 Biological Process (GOBP) gene set collections from the Molecular Signatures Database
601 (MSigDB).(55-57) The hallmark collection includes 50 gene sets, with clearly defined gene
602 expression, as a high-level representation of a compilation of other gene sets in MSigDB, whereas
603 GOBP represents >7000 gene sets capturing biological processes. A normalized enrichment
604 score (|NES|>1.5) and an adjusted p-value cutoff (FDR<0.05) were used to determine significantly
605 altered pathways between Q331K TBI and WT TBI mice. NES is the normalized enrichment
606 score, which reflects the overrepresentation of a gene set at the upper (positive value) or lower
607 (negative value) end of a ranked gene list. GSEA analysis of the hallmark collection identified
608 “mammalian target of rapamycin complex 1 (MTORC1) signaling” as the top upregulated gene
609 set (**Fig. 2B**; **Supp. Table II**). MTORC1 signaling is involved with multiple cellular processes,
610 including protein synthesis and autophagy.(70) Protein folding was associated with the top 3 gene
611 sets from GOBP identified in the GSEA analysis (**Fig. 2C**). The relative expression for the top 30
612 ranked genes in the “MTORC1 signaling” (**Fig. 2D**) and “protein folding” (**Fig. 2E**) pathways are
613 shown in a heatmap representation, highlighting striking differences in gene expression between

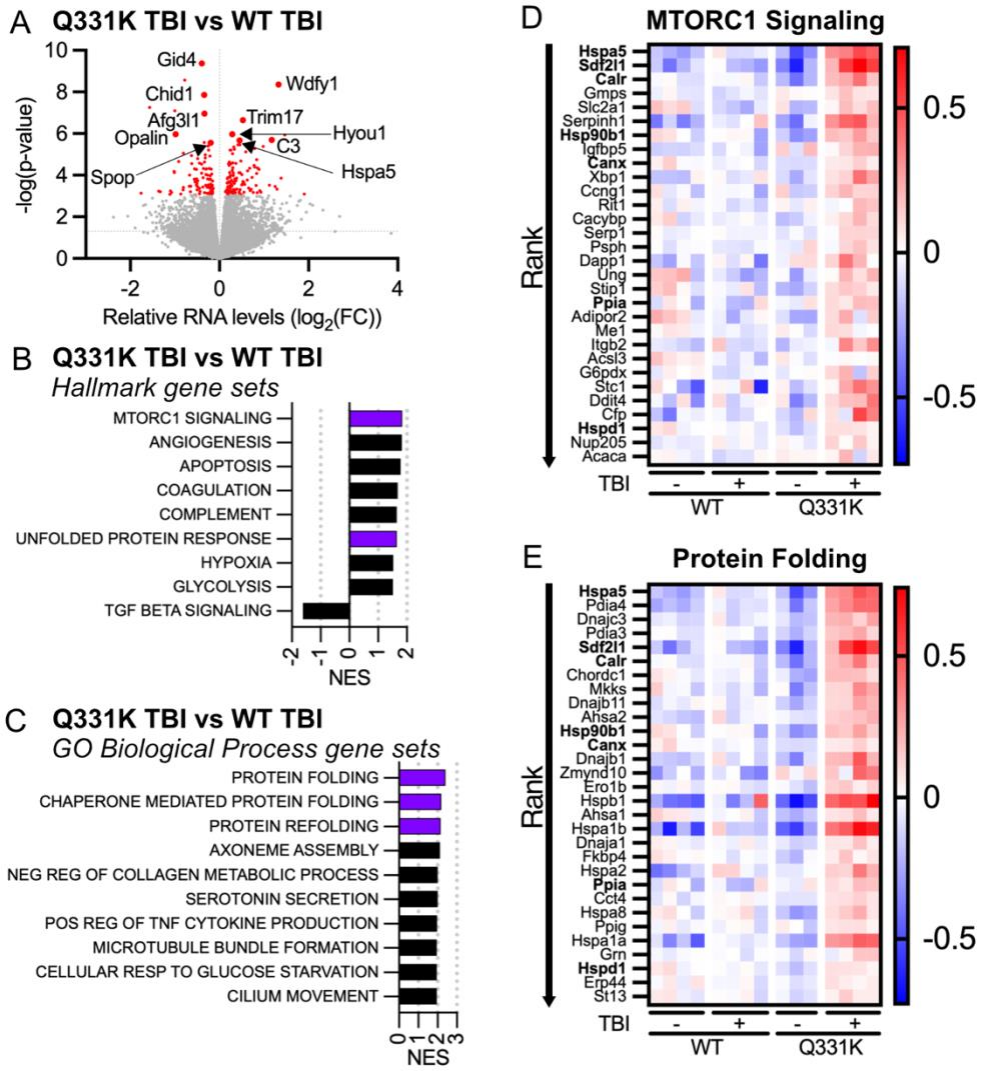

Figure 2. Upregulation of MTORC1 and protein folding genes in Q331K versus WT mouse brain after TBI. (A) Volcano plot of RNAseq data comparing Q331K and WT mice, each with either TBI or sham surgery. Differentially expressed genes (DEGs) with FDR <0.1 are shown in red. Top up- and down-regulated annotated genes are labeled. **(B,C)** Top GSEA gene set hits (both up and down regulated, as applicable) for Q331K TBI relative to WT TBI using the Molecular Signatures Database (MSigDB) hallmark **(B)** and Gene Ontology Biological Process **(C)** collections. Purple bars denote gene sets associated with proteostasis. **(D,E)** Heatmaps showing the top 30 ranked genes in the hallmark gene set "MTORC1 signaling" **(D)** and the Gene Ontology Biological Process gene set "protein folding" **(E)**. The $\log_2$(fold change) relative to the mean expression is shown for each sample. All pathway hits meet cutoff criteria of

624 FDR <0.05 and |NES|>1.5. Genes in both “MTORC1 signaling” and “protein folding” gene sets are indicated
625 in bold.
626
627
628
629
630
631
632
633
634
635
636
637
638
639
640
641
642
643

644 Q331K TBI mice relative to the other three cohorts. Seven genes overlap between the top ranked
645 list for MTORC1 signaling and protein folding, with *Hspa5*, encoding the endoplasmic reticulum
646 (ER)-associated chaperone heat shock 70 kDa protein 5, as the top ranked gene in both pathways
647 (**Fig. 2D-E**).

648 To further examine differentially expressed genes between Q331K and WT mice as a function of
649 TBI, we compared significant transcriptional changes in Q331K TBI versus Q331K sham mouse
650 brain lysates (**Fig. S2A and Supp. Table I**) with those in WT TBI versus WT sham (**Fig. S2B and**
651 **Supp. Table I)** by plotting data with directional p-values (**Fig. 3A**), where the p-value is plotted as
652 a negative number to reflect a decrease in gene expression for a specific comparison and as a
653 positive number to reflect an increase in expression. In this plot, genes that significantly change
654 in expression in the Q331K TBI versus Q331K sham comparison (sections shaded in pink) can
655 be visualized along the x-axis, whereas the y-axis highlights genes that significantly change in
656 expression in WT TBI versus WT sham mice (sections shaded in blue). Sections shaded in grey
657 highlight genes that are differentially expressed as a function of TBI, irrespective of genotype (**Fig.**
658 **3A**), and include 63 genes with FDR<0.1 in both comparisons (**Fig. 3B, Supp. Table I**). GSEA
659 hallmark pathway analysis revealed "TNFa signaling via NFkB" as the top ranked, upregulated
660 pathway in both Q331K (**Fig. 3C and Fig. S2C**) and WT (**Fig. 3D and Fig. S2D**) brain lysates
661 post-TBI relative to their sham counterparts (**Supp Table II**). This is not surprising, given that
662 inflammation and changes in innate immunity-related processes are well-documented following
663 brain trauma.(71) Pathway changes that were specific to the WT TBI versus WT sham comparison
664 indicate a downregulation of metabolic and bioenergetic processes that occur in the mitochondria,
665 such as "oxidative phosphorylation" and "NADH dehydrogenase complex assembly" (**Fig. 3D,E**
666 **and Fig. S2E,F**). TBI is known to affect mitochondrial bioenergetics, where TBI induces
667 mitochondrial damage and results in reduced energy production.(72) Although these pathways
668 were not significantly altered between Q331K TBI and Q331K sham brain lysates, expression of

669 genes in these pathways were variable and potentially dysregulated in Q331K mice under both
670 TBI and sham conditions, an observation that may reflect transient and adverse effects of mutant
671 TDP-43 on mitochondria reported by others.(73)

672 Strikingly, nine out of the top ten GOBP pathways emerging from the Q331K TBI versus Q331K
673 sham comparison were proteostasis-related, including protein folding and response to ER-stress
674 (**Fig. 3F**), which were not enriched pathways in the WT TBI versus WT sham comparison (**Fig.**
675 **3D, Supp Table II**). Further, proteostasis-related genes *Hspa5*, mesencephalic astrocyte-derived
676 neurotrophic factor (*Manf*), calreticulin (*Calr*) and protein disulfide isomerase family A, members
677 3 (*Pdia3*) and 6 (*Pdia6*) were significantly increased in Q331K TBI versus Q331K sham mice (**Fig.**
678 **3A**; pink-shaded region). Proteostasis-related gene expression changes did not persist long-term
679 post-TBI, as determined by a separate RNA-seq analysis on whole brain mouse lysates 7-months
680 post-TBI or sham surgery, for both WT and Q331K mice. In fact, there were no significant gene
681 expression changes (at cutoff FDR < 0.1) due to TBI for either genotype (i.e., Q331K TBI versus
682 Q331K sham and WT TBI versus WT sham; **Supp Table I**).

683 Considering the upregulation of transcripts involved in protein folding and ER-stress in Q331K
684 mice 24h post-TBI compared to the other three cohorts, we assessed protein level changes with
685 quantitative proteomics analysis of mouse brain lysates labeled with tandem mass tags (TMTs)
686 from the four cohorts. Other than TDP-43, no significantly upregulated proteins were detected
687 (**Fig. S3A, Supp Table III**). In fact, TDP-43 upregulation was observed in Q331K versus WT
688 comparisons irrespective of surgery type, at both mRNA and protein levels (**Fig. S3C,D**),
689 consistent with a loss of TDP-43 autoregulation due to the Q331K mutation.(44) Despite a
690 significant upregulation of *Hspa5* at the mRNA level in Q331K TBI mice, differential expression of
691 Hspa5 protein was not observed across the four mouse cohorts (**Fig. S3B)**. We additionally
692 probed for isoforms of active X-box binding protein 1 (Xbp1; **Fig. 2D**), which becomes spliced
693 (Xbp1s) and activated under conditions of ER-stress (**Fig. 3F**),(74) by Western blot analysis.

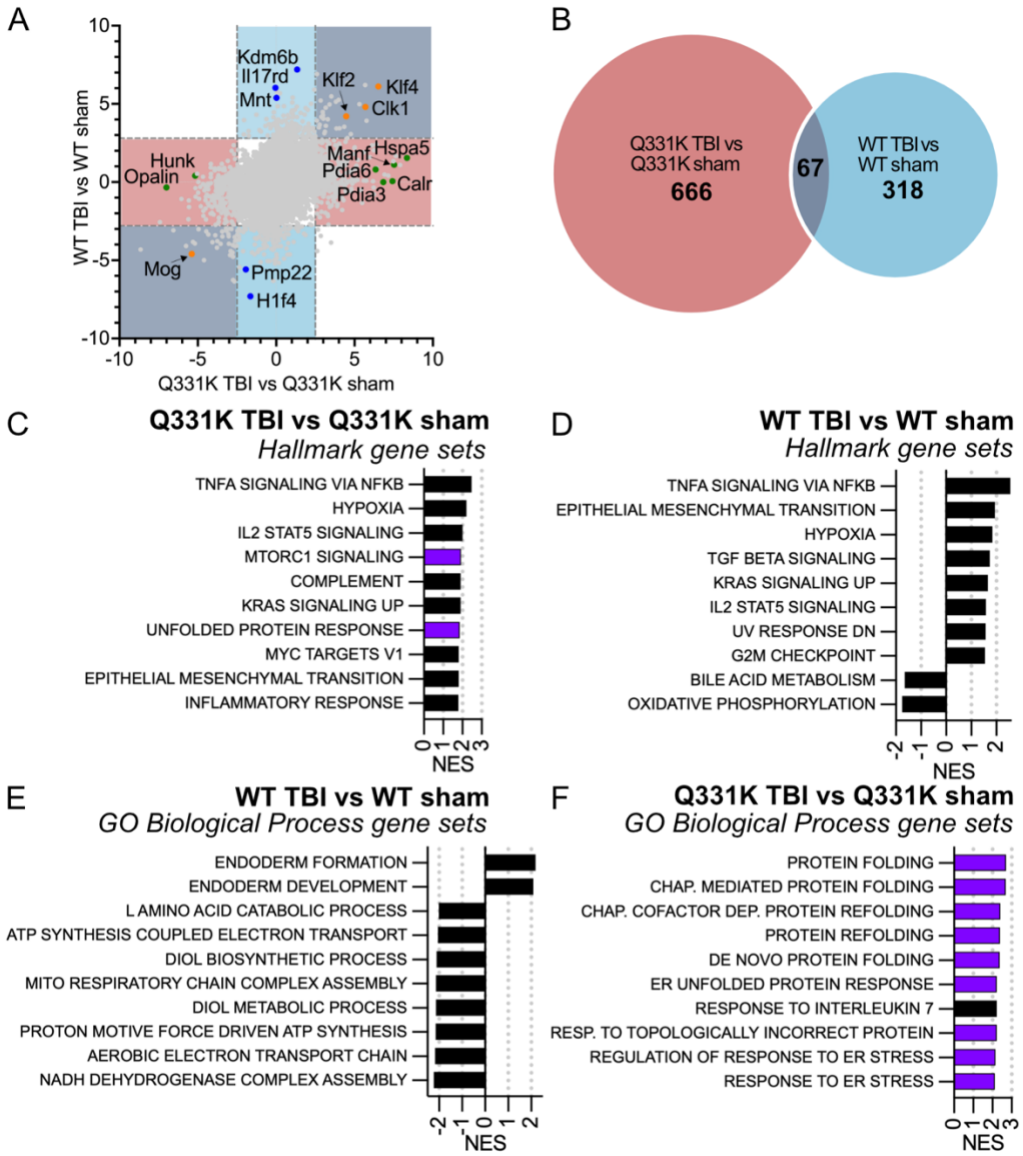

Figure 3. Differentially expressed genes in WT and Q331K mouse brain as function of surgery. (A) Plot of directional nominal p-values (-log) from transcriptomics datasets for the WT TBI versus WT sham comparison plotted against the Q331K TBI versus Q331K sham comparison. The sign of the log10p score reflects the direction of the fold change. Orange dots denote genes with expression changes specifically due to TBI, irrespective of genotype. Blue and green dots denote genes with expression changes specifically in WT and Q331K mice, respectively, after TBI. Color-shaded sections indicate unique and overlapping gene changes, as illustrated in B. Dotted lines indicate FDR=0.1 **(B)** Venn diagram illustrating minimal gene overlap between Q331K and WT mice subjected to TBI using FDR <0.1. **(C-F)** Top GSEA gene set hits from the RNAseq analysis for Q331K TBI versus Q331K sham conditions using the hallmark

704 collection **(C)**, WT TBI versus WT sham conditions using the hallmark collection **(D)**, WT TBI versus WT
705 sham conditions using the Gene Ontology Biological Process collection **(E)** and Q331K TBI versus Q331K
706 sham conditions using the Gene Ontology Biological Process collection **(F)**. All gene set hits meet cutoff
707 criteria of FDR <0.05 and |NES|>1.5. Purple bars denote pathways that are associated with proteostasis.
708
709
710
711
712
713
714
715
716
717
718
719
720
721
722
723
724

725 Xbp1s was not detected in samples from any mouse cohort and levels of unspliced Xbp1 (Xbp1u)
726 were unchanged across conditions (**Fig. S3E**). The apparent lack of upregulation at the protein
727 level may be due to deficits in protein synthesis or because 24h post-TBI is too early a timepoint
728 for detection of newly translated protein. Nonetheless, the transcriptomics data clearly indicate a
729 robust upregulation of proteostasis-related pathways at the mRNA level that is dependent on both
730 TBI and expression of mutant TDP-43.

731 To gain insight into the relevance of our TBI model to neurodegenerative diseases such as ALS
732 and FTLD-TDP, we compared the GSEA hallmark gene set analyses of the TBI versus sham
733 conditions for both WT and Q331K mice with recent transcriptomic analyses of human ALS post-
734 mortem spinal cord and FTLD-TDP brain tissues.(45, 75) Significantly upregulated pathways in
735 FTLD-TDP and/or ALS CNS tissues, such as “TNFa signaling via NFkB” and “hypoxia”, were also
736 significantly upregulated in our TBI model, irrespective of genotype (**Fig. S4**). Notably, several
737 significantly upregulated pathways in FTLD-TDP and/or ALS CNS post-mortem tissues were only
738 observed in Q331K mice after TBI, but not WT mice after TBI, including “MTORC1 signaling”,
739 “unfolded protein response” and “inflammatory response” (**Fig. S4**). Similarly, GO terms related
740 to cytoplasmic translation and innate immunity emerged from a single nucleus sequencing
741 analysis of neurons from a separate study of human post-mortem ALS and FTLD brain tissue.(76)
742 Therefore, there appears to be a synergistic effect of mutant TDP-43 dysfunction and acute brain
743 trauma on biological processes in the CNS that, at least partially, recapitulates neurodegenerative
744 disease processes on the ALS/FTLD spectrum.

745 **Proteostasis-related factors and pathways are downregulated in mutant TDP-43 mice at**
746 **baseline.** We performed similar omics analyses on cohorts of WT and Q331K mice without TBI,
747 including RNA-seq on mice without surgery (i.e., naïve mice). In our view, the sham condition
748 represents the most relevant control for TBI, as it accounts for gene expression changes that
749 occur from the surgery itself, thereby revealing expression changes due to the impact. Including

750 naïve mice here serves as an additional control for identifying differentially expressed genes due
751 to expression of mutant TDP-43. For the Q331K versus WT sham comparison, only two
752 downregulated pathways emerged from our GSEA analysis, “protein folding” and “aerobic
753 electron transport chain” (**Supp. Table II**). Similarly, “MTORC1 signaling”, which includes
754 proteostasis-related genes, such as heat shock protein family chaperones *Hspd1*, *Hspe1*, and
755 *Hspa4*, was a downregulated pathway for the Q331K versus WT naïve comparison (**Supp. Table**
756 **II**). Plotting transcriptomics data with directional p-values for the Q331K versus WT sham groups
757 against Q331K versus WT naïve groups revealed a significant downregulation of genes involved
758 in the ubiquitin-proteosome pathway, including glucose-induced degradation protein 4 homolog
759 (*Gid4*) and speckle-type POZ protein (*Spop*), the latter a downregulated gene that was also
760 observed by White et al. in this Q331K model (**Fig. S5B** and **Supp. Table IV**).(44) Of note, both
761 *Gid4* and *Spop* remain downregulated in Q331K sham and TBI mice at 7 months post-TBI relative
762 to WT groups (**Supp. Table I, Fig. S5C,D**). Further, our quantitative proteomics analysis of Q331K
763 versus WT sham groups uncovered a modest yet significant decrease in the large ribosomal
764 subunit protein P1 (Rplp1), which plays a critical role in embryonic and brain development (**Fig.**
765 **S3F**, **Supp. Table III**).(77) Collectively, these omics data point toward a deficit in proteostasis-
766 related pathways in Q331K mice at baseline.

767 **TDP-43 exhibits altered nuclear and cytoplasmic localization following TBI.** Different TBI
768 models reportedly induce subcellular redistribution of TDP-43 from the nucleus, where the protein
769 is predominately expressed under homeostatic conditions, to the cytoplasm.(13, 37-41)
770 Enhanced cytoplasmic localization of TDP-43 is also well-documented in other stress paradigms
771 in vivo and in vitro, indicating that subcellular redistribution of TDP-43 represents a physiological
772 response to stress.(2-6, 78) Given the disparate responses between Q331K and WT mice to TBI
773 (**Figs. 1-3**), we examined the cellular localization of TDP-43 in situ as a function of surgery and
774 TDP-43 genotype. Mouse brain tissue sections from TBI and sham cohorts were stained with anti-

775 TDP-43 antibody and counterstained with DAPI. Obvious changes in subcellular TDP-43
776 distribution were observed in the cortex, amygdala, and hypothalamus (regions defined in **Fig.**
777 **1B**) of both Q331K and WT mice (**Fig. 4**), whereas changes in TDP-43 subcellular distribution
778 were minimal or not detected in other regions of the tissue section (not shown). Sham animals
779 also exhibited some degree of cytoplasmic TDP-43 redistribution in these brain regions, possibly
780 indicative of cellular "stress" caused by the sham surgery, and therefore the naïve condition was
781 included here for further analysis.

782 To quantify TDP-43 cellular localization, confocal microscopy images were acquired within the
783 cortex, amygdala, and hypothalamus of Q331K and WT mice in the absence of surgery (i.e.,
784 naïve) or 24h after receiving a sham or TBI surgery, for a total of six groups (**Fig. 4A,B**). First,
785 TDP-43 nuclear-to-cytoplasmic (N/C) ratios were determined for all cells across a field of view
786 (FOV) on a per image basis. Reductions in TDP-43 N/C in TBI versus naïve conditions were
787 generally observed in all three brain regions for both WT and Q331K mice, although some
788 comparisons did not reach statistical significance (**Fig. S6A**). Notably, TBI-induced reductions in
789 TDP-43 N/C ratios occurred in both ipsilateral (i.e., TBI side) and contralateral hemispheres of
790 the brain (**Fig. S6A**) and were prominent in the amygdala and hypothalamus. Therefore, the
791 effects of TBI on subcellular TDP-43 localization extend beyond the site of injury in the cortex,
792 likely because the weight-drop induces contact between the skull and brain tissue at the base of
793 the skull (**Fig. 1A,B**). TBI-induced changes in TDP-43 subcellular localization represented an
794 acute response to TBI, as differences in TDP-43 N/C ratios were no longer observed at 5-months
795 post-surgery (**Fig. S7**).

796 As changes in TDP-43 subcellular localization were not observed in every cell, the percentage of
797 cells exhibiting reduced TDP-43 N/C ratio relative to the naïve condition was determined from the
798 FOVs above. Q331K TBI mice exhibited a significantly higher percentage of cells with reduced

799 TDP-43 N/C ratio in all three brain regions relative to Q331K naïve mice for both ipsilateral and

800 contralateral hemispheres, which was collectively a more robust change than for their WT

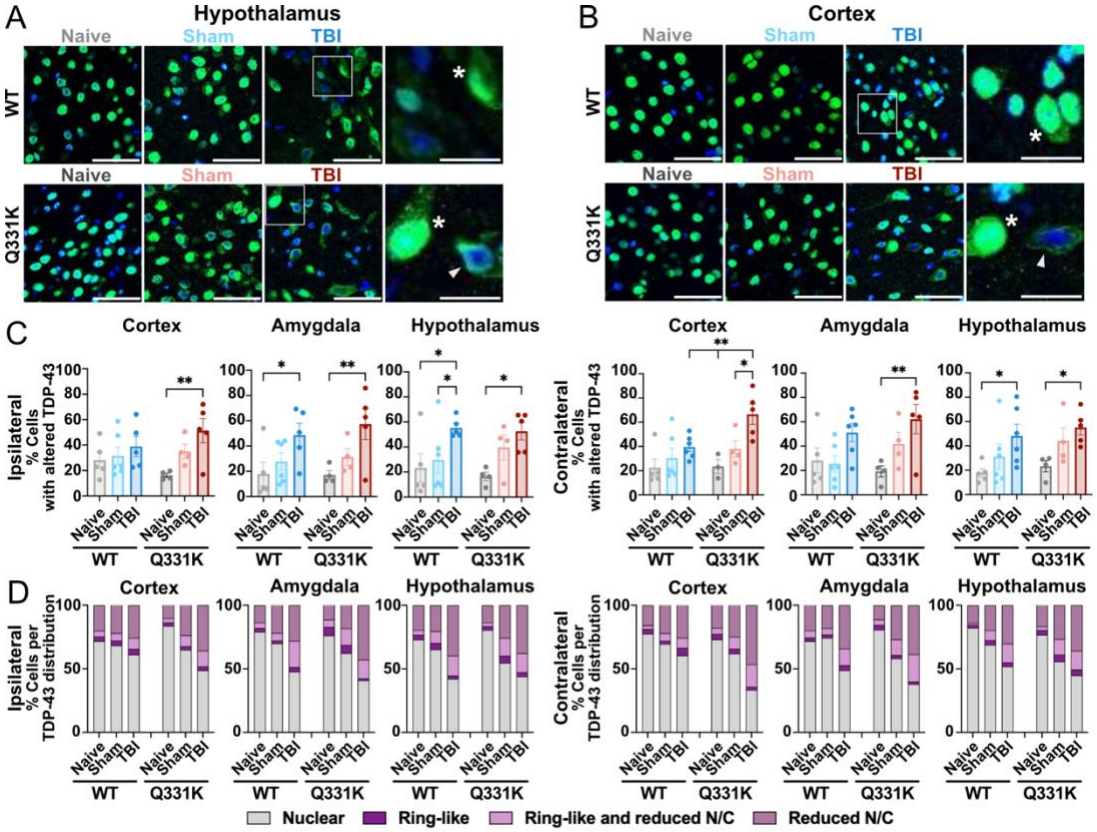

801

802 **Figure 4. Alterations in TDP-43 localization in WT and Q331K mice as a function of surgery. (A-B)**

803 Confocal immunofluorescence images from WT and Q331K mice under native (i.e., no surgery) conditions

804 or 24h post-surgery (sham and TBI). Tissues were stained for TDP-43 (green) and counterstained with

805 DAPI (blue). Images from the hypothalamus (A) and cortex (B) are shown. Cropped insets highlight cells

806 with cytoplasmic (asterisks) and ring-like distribution (triangles) of TDP-43 under conditions of TBI. Scale

807 bar=50 um in the low magnification image and =20 um in the insets. **(C)** Percent of cells that exhibit altered

808 TDP-43 localization (ring-like, reduced nuclear-to-cytoplasmic (N/C) ratio, or both) in the cortex, amygdala,

809 or hypothalamus, either ipsilateral (left) or contralateral (right) to the impact site 24h post-surgery. (**D)**

810 Stacked bar graphs representing the average percent of cells that exhibit nuclear TDP-43 localization (grey)

811 or a type of altered TDP-43 localization (defined in C and color-coded according to the key) within the

812 indicated brain region. **(C-D)** Quantification of TDP-43 localization was performed using tissues from n=4-

813 6 mice, where each dot represents a different mouse. Statistical analysis was performed using two-way
814 ANOVA followed by Tukey's multiple comparisons test: *p<0.05, **p<0.01, ***p<0.001, ****p<0.0001.

815 counterparts (**Fig. S6B**). During this analysis, we also noticed a "ring-like" TDP-43 staining
816 pattern, which appeared as dense TDP-43 signal near the outer edge of (but still within) the
817 nucleus (**Fig. 4A**, Q331K inset) and that also occurred in cells with cytoplasmic TDP-43 staining.
818 We developed a CellProfiler pipeline (see Methods) to quantify the percentage of cells with this
819 phenotype and found significant ring-like TDP-43 staining in TBI versus control comparisons in
820 all brain regions for at least one genotype (**Fig. S6C**). Ring-like TDP-43 staining was most
821 prominent in the hypothalamus and amygdala for both Q331K TBI and WT TBI mice versus their
822 respective controls, on both sides of the brain (**Fig. S6C**).

823 To assess the full extent of altered TDP-43 subcellular localization after TBI, we compiled the
824 data above (**Fig. S6**) and determined the percentage of cells exhibiting reduced TDP-43 N/C ratio
825 and/or ring-like TDP-43 (**Fig. 4C,D**). TBI induced more pronounced changes in TDP-43
826 localization in the cortical region below the impact site in Q331K versus WT mouse brain,
827 particularly on the contralateral side (**Fig. 4C,D**). These analyses also highlighted that Q331K
828 sham animals exhibited significant TDP-43 subcellular localization changes that were more
829 similar to the Q331K TBI condition and were significantly different than their Q331K naïve
830 counterparts, especially in the hypothalamus (**Fig. S6B,C**). Taken together, these data
831 demonstrate an acute response involving the TDP-43 protein to brain injury that occurred
832 irrespective of genotype. That Q331K mice appeared to be more sensitive to both sham and TBI
833 surgery with respect to changes in subcellular TDP-43 localization further supports the notion that
834 TDP-43 dysfunction leads to altered stress responses in vivo.

835 **Effects of TDP-43 mutation and TBI on select TDP-43 splice targets.** An important nuclear
836 function of TDP-43 involves the alternative splicing of conserved exons for numerous RNA
837 targets,(1) which can become mis-spliced as a result of TDP-43 knock-down, overexpression

838 and/or mutation.(79, 80) We therefore considered whether TBI-induced subcellular redistribution
839 of TDP-43 (**Fig. 4** and **Fig. S6**) would manifest in altered splicing of TDP-43 RNA targets. To
840 address this possibility, we probed for potential changes in splicing patterns for eight known RNA
841 targets of TDP-43 within mouse brain lysates derived from near the TBI site (**Fig. 1A**) using RT-
842 PCR and primer sequences that cover the exon junctions of interest (**Supp. Table V**). TDP-43
843 RNA targets included several that become mis-spliced due to TDP-43 misexpression, including
844 DnaJ heat shock protein family (Hsp40) member 5 (*Dnajc5*), potassium voltage-gated channel
845 interacting protein 2 (*Kcnip2*), protein phosphatase 3 catalytic subunit alpha (*Ppp3ca*), and
846 translin (*Tsn*).(81-84) Splicing patterns were assessed by gel electrophoresis (**Fig. 5A**) and
847 reported as the fraction of the mis-spliced variant versus the common or more abundant variant
848 expressed under normal conditions (**Fig. 5B**). For *Dnajc5*, no differences in splicing of exon 5
849 were observed between the mouse groups studied herein. In contrast, enhanced exon exclusion
850 most consistent with TDP-43 loss-of-function was detected for Q331K mice, irrespective of
851 surgery, for *Kcnip2* (exon 3 only, indicated by an increase in S1), *Ppp3ca* and *Tsn*.(84) Consistent
852 with TDP-43 gain-of-function reported in this and other Q331K mouse models,(44, 82) enhanced
853 exclusion of exon 17b in Sortilin-1 (*Sort1*) was observed in both Q331K TBI and sham mice; in
854 contrast, inclusion of exon 17b correlates with TDP-43 loss-of-function.(29, 81-83)
855
856 We examined additional genes that are prone to exon skipping, referred to as skiptic exons,
857 caused by mutant TDP-43 gain-of-function in vivo.(80, 82) These included parkin coregulated like
858 (*Pacrgl*), solute carrier family 6 member 6 (*Slc6a6*) and ubiquitin protein ligase E3C (*Ube3c*).(82)
859 Skiptic exons were detected in Q331K samples for all three genes. Intriguingly, the skiptic exon
860 in *Ube3c* was attenuated in Q331K mice after TBI, thus representing a gene-splicing event that
861 was modulated by TBI, specifically in Q331K mice (**Fig. 5A,B**). *Ube3c* encodes an E3 ubiquitin
862 ligase that promotes proteasomal degradation of misfolded proteins.(85) TDP-43-mediated
863 skipping of exon 6 in *Ube3c* causes the removal of 54 amino acid residues between the ubiquitin-

binding domain and the catalytic Homologous to the E6-AP Carboxyl Terminus (HECT) domain (**Fig. S8A**). While the impact of exon 6 removal on Ube3c function is unknown,(82) modeling the 3-dimensional protein structure of Ube3c in AlphaFold(65) suggests that omission of exon 6 could induce conformational

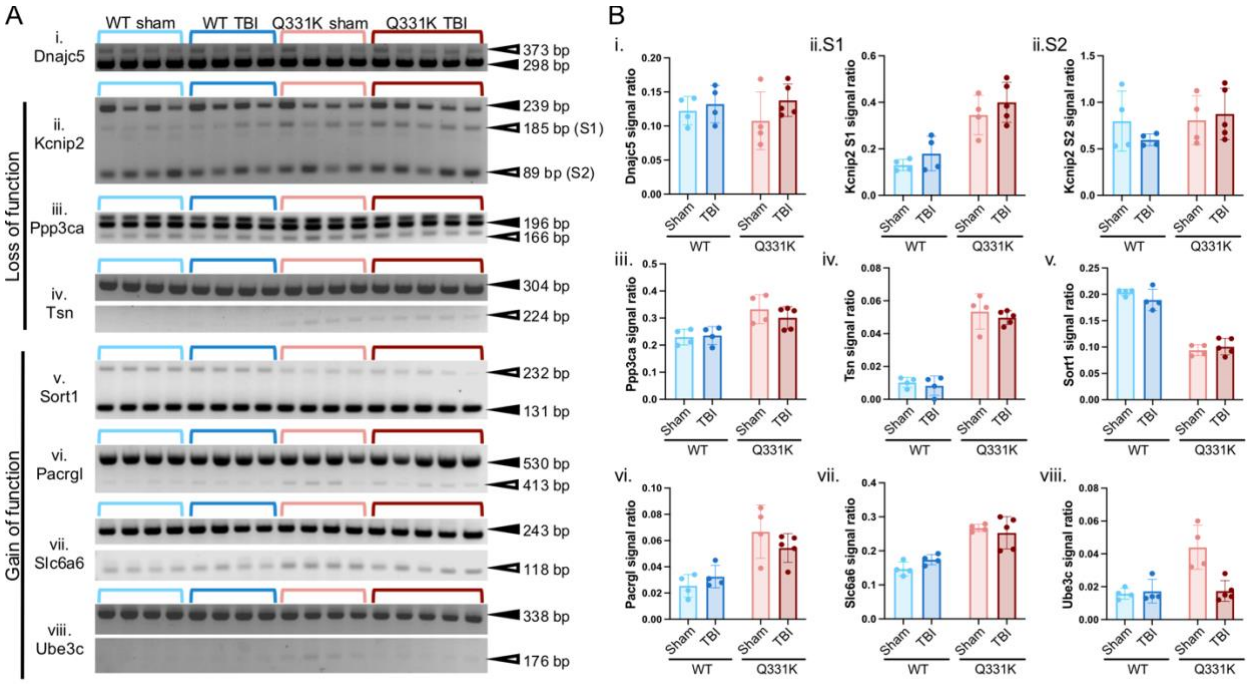

Figure 5. **Alternative splicing patterns for TDP-43 targets in WT and Q331K mouse brain after TBI.** **(A)** Splice variants of known TDP-43 RNA targets (i-vi) detected by RT-PCR analysis in WT and Q331K mice 24h after either TBI or sham surgery. The PCR primers, exons of interest and references for the primers used in this study are shown in **Supp Table VI**. Splicing patterns that are consistent with TDP-43 loss of function or gain of function are indicated. Common and mis-spliced variants are denoted by, respectively, closed and open arrowheads with the corresponding size (bp=base pairs) of the PCR product. Gels are representative of at least n=3 separate RT-PCR experiments. **(B)** Densitometry analysis of the gels in (A) was used to determine the ratio of the mis-spliced/common PCR product for each gene of interest. Each dot in the graph represents a separate mouse.

881

882

883

884 perturbations in the protein N-terminal to the HECT domain (**Fig. S8B**). The effects of TBI on
885 *Ube3c* exon 6 skipping in Q331K mice were acute, as exon skipping was no longer observed at
886 7-months post-TBI. Additionally, the splicing patterns for the other seven candidate TDP-43
887 mRNA targets were unchanged at 7-months post-TBI compared to 24h post-TBI (**Fig. S9**). Taken
888 together, these RT-PCR results indicate that TBI-induced changes in subcellular TDP-43
889 localization do not strongly correlate with a loss of TDP-43 splicing function, as most of the
890 observed splicing differences were due to TDP-43 mutation and not TBI. An exception is TDP-43
891 Q331K-induced skipping of exon 6 in *Ube3c*, which is attenuated during the acute phase post-
892 TBI.

893

894 **Ribosomal proteins exhibit thermal instability in Q331K mice.** A cytoplasmic shift in TDP-43
895 localization appears to represent a physiological response to brain trauma in mice, irrespective of
896 TDP-43 genotype (**Fig. 4**). We hypothesized that mutations in TDP-43 could alter the nature of
897 this response by perturbing cytoplasmic cellular processes involved in stress recovery. For
898 example, disease-linked mutations in TDP-43 have been shown to affect the interaction of TDP-
899 43 with cytoplasmic RNA granules as well as the biophysical properties of these granules.(11, 12,
900 14-16) Here, we examined protein content and protein thermostability of mouse brain lysates in
901 both WT and Q331K mice after sham or TBI surgery using the Proteome Integral Solubility
902 Alteration (PISA) assay (**Fig. S10A**) coupled with TMT quantitative proteomics using mass
903 spectrometry.(86, 87) PISA capitalizes on the principle that proteins become insoluble when
904 denatured. By extension, how a protein partitions between the soluble and insoluble fraction as a
905 function of temperature can be used to detect changes in protein thermostability under various
906 conditions. PISA and similar assays were historically used to elucidate protein targets of small

907 molecules, which generally induce an increase in thermostability of their protein targets upon
908 binding.(86, 88) We reasoned that PISA could be repurposed here for identifying thermostability
909 shifts of cytosolic proteins and protein complexes in brain lysates as a function of TBI and TDP-
910 43 mutation. To simplify sample processing and analysis, lysates were first depleted of large
911 organelles. A Western blot analysis with histone H3 and cytochrome c oxidase subunit IV (CoxIV)
912 antibodies confirmed that this protocol depleted nuclei and mitochondria, respectively, whereas
913 anti-calreticulin confirmed that ER was retained (**Fig. S10B**).

914 For the PISA assay, lysates were subjected to a narrow temperature gradient (52-54°C) followed
915 by centrifugation to remove the insoluble protein (**Fig. S10A**). The resulting soluble fraction was
916 subjected to quantitative proteomics (**Fig. S10C**). In parallel, quantitative proteomics was
917 performed on cytosolic lysates without heat exposure to determine total protein levels (**Fig.**
918 **S10D**). Only modest differences in total protein levels between Q331K TBI and WT TBI cytosolic
919 lysates were detected by the proteomic analysis (**Fig. S10D and Supp. Table VI)**, for which no
920 pathways were significantly enriched by GSEA (**Supp. Table VII**). In striking contrast, GSEA
921 analysis of the PISA proteomics for the Q331K TBI versus WT TBI comparison revealed multiple
922 downregulated processes, with seven of the top ten GOBP hits including terms for translation and
923 ribosome (**Fig. 6A**). As shown in the heatmap for "cytoplasmic translation" (**Fig. 6B**), ribosomal
924 proteins account for most of the top 30 proteins in this pathway. Proteins in the "cytoplasmic
925 translation" pathway become elevated within the soluble fraction from WT animals after TBI
926 compared to their sham counterparts, as demonstrated in the heatmap (**Fig. 6B**) and a box plot
927 for the top five ranked proteins in the heatmap, all of which are ribosomal proteins (**Fig. 6C**).
928 Conversely, these ribosomal proteins are diminished within the soluble fraction from Q331K sham
929 mice relative to WT mice, and while they do become enhanced after TBI, their levels remain
930 significantly below that of WT TBI lysates (**Fig. 6B,C**).

931 Considering that decreased protein solubility in the PISA assay is indicative of reduced protein
932 thermostability, our interpretation of the PISA outcomes is that ribosomal proteins and potentially
933 ribosome complexes themselves exhibit reduced thermostability in Q331K mice relative to WT
934 mice. Polysome profiling of cytosolic lysates confirmed that intact 80S ribosomes were indeed
935 present for both WT and Q331K conditions (**Fig. S11A-C**). RNA fragment analysis of isolated
936 RNA confirmed the presence of both 28S and 18S ribosomal RNA (**Fig. S11D**). Given that the
937 effect of TDP-43 Q331K expression on ribosome stability occurred irrespective of surgery, we
938 assessed the main effects of genotype for additional proteomic analyses. This approach further
939 verified that total levels of ribosomes in the cytosolic lysates were unchanged between TDP-43
940 genotypes (**Fig. 6D**), but that their thermostability was reduced in Q331K mice relative to WT mice
941 (**Fig. 6E**). We note that Rplp1, which was reduced in the proteomics analysis of total brain lysates
942 (**Fig. S3F**), was not quantifiable in the cytosolic proteomics because only one unique peptide was
943 identified whereas ≥2 were required in our pipeline for protein level quantification (**Supp. Table**
944 **VI**)**.** A subsequent STRING analysis using Markov Clustering (MCL) for the 50 destabilized
945 proteins (FDR < 0.1) revealed a major cluster of 27 proteins (Cluster 1) associated with
946 "cytoplasmic translation" and "ribosome" (**Fig. 6F**).(89, 90) Importantly, most of the ribosomal
947 proteins in this cluster were shown to immunoprecipitate with TDP-43 from cultured cell and/or
948 mouse brain lysates, raising the possibility that association of mutant TDP-43 with ribosomes
949 and/or ribosomal proteins could impact ribosome stability.(18, 91, 92) For the polysome profiling
950 study, we noticed that the absorbance at 254nm was consistently lower for Q331K cytosolic
951 lysates relative to that of WT within the peak where medium polysomes elute from the gradient
952 (**Fig. S11B**). Additionally, we observed a subpopulation of TDP-43 associating with the 80S
953 ribosome (**Fig. S11C**). These observations suggest that translation efficiency may be reduced in
954 Q331K mouse brain relative to WT mice. "Cluster 2", the second largest cluster revealed by
955 STRING, includes multiple proteins involved in protein folding such as heat shock 70 kDa protein
956 4 (Hspa4) and four of the eight subunits that comprise the eukaryotic cytosolic T-complex protein

957 1 (TCP-1) ring complex or chaperonin containing TCP-1 (TRiC/CCT), including Tcp1/Cct1, Cct6a,
958 Cct7 and Cct8. Interestingly, Cheng et al. identified these as putative TDP-43 interactors.(91)
959 TRiC/CCT plays important roles in maintaining proteostasis and ensuring the proper folding of
960 critical cellular

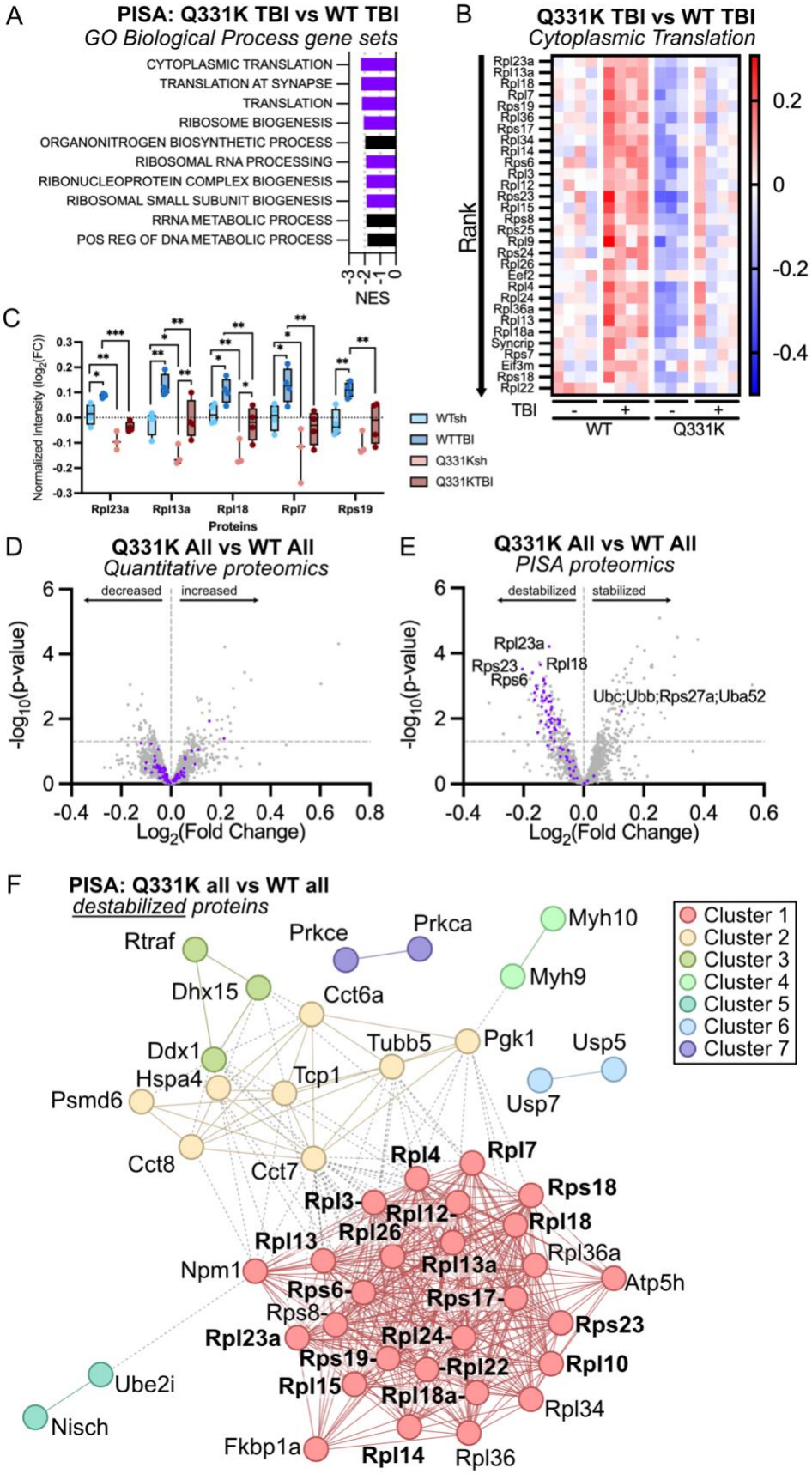
A
PISA: Q331K TBI vs WT TBI
GO Biological Process gene sets
CYTOPLASMIC TRANSLATION
TRANSLATION AT SYNAPSE
TRANSLATION
RIBOSOME BIOGENESIS
ORGANONITROGEN BIOSYNTHETIC PROCESS
RIBOSOMAL RNA PROCESSING
RIBONUCLEOPROTEIN COMPLEX BIOGENESIS
RIBOSOMAL SMALL SUBUNIT BIOGENESIS
RRNA METABOLIC PROCESS
POS REG OF DNA METABOLIC PROCESS
NES
B
Q331K TBI vs WT TBI
Cytoplasmic Translation
Rank
TBI
WT
Q331K
C
Normalized Intensity (log2(FC))
Rpl23a
Rpl13a
Rpl18
Rpl7
Rps19
Proteins
WTsh
WTTBI
Q331Ksh
Q331KTBI
D
Q331K All vs WT All
Quantitative proteomics
decreased
increased
-log10(p-value)
Log2(Fold Change)
E
Q331K All vs WT All
PISA proteomics
destabilized
stabilized
Rpl23a
Rps23
Rpl18
Rps6
Ubc;Ubb;Rps27a;Uba52
F
PISA: Q331K all vs WT all
destabilized proteins
Cluster 1
Cluster 2
Cluster 3
Cluster 4
Cluster 5
Cluster 6
Cluster 7
Rtraf
Prkce
Prkca
Myh10
Myh9
Dhx15
Cct6a
Tubb5
Pgk1
Usp5
Ddx1
Hspa4
Tcp1
Psmd6
Usp7
Cct8
Cct7
Rpl4
Rpl7
Rps18
Rpl3
Rpl12
Rpl18
Rpl13
Rpl26
Rpl36a
Npm1
Rpl13a
Atp5h
Rps6
Rps17
Rps8
Rps23
Rpl23a
Rpl24
Rpl10
Rps19
Rpl22
Ube2i
Rpl15
Rpl18a
Rpl34
Nisch
Fkbp1a
Rpl14
Rpl36

961

962 **Figure 6. PISA analysis identifies melting temperature shifts in ribosomal and chaperonin proteins**
963 **in Q331K mouse brain lysates. (A)** Top 10 pathway hits with GSEA enrichment of thermostability changes
964 in Q331K TBI versus WT TBI brain lysates using GOBP. Purple bars denote pathways involved in ribosome
965 biology. **(B)** Heatmap showing levels of soluble protein detected by PISA for the top proteins in the pathway
966 "Cytoplasmic Translation". The $\log_2$(fold change) relative to the mean expression is shown for each sample.
967 **(C)** Box plot of top-ranking proteins in the "Cytoplasmic Translation" gene set for the indicated condition.
968 **(D,E)** Volcano plot for the quantitative proteomics (**D**) and PISA (**E**) results for Q331K ("Q331K All") versus
969 WT ("WT All"), where TBI and sham conditions are combined for each genotype. Ribosomal proteins are
970 highlighted as purple dots. (**F**) Results of a STRING analysis using the Markov Cluster Algorithm showing
971 significantly destabilized proteins (FDR < 0.1) in the "Q331K All" versus "WT All" comparison. Key terms
972 included for each cluster are as follows. Cluster 1: cytoplasmic translation, Signal Recognition Particle
973 (SRP)-dependent co-translational protein targeting to membrane, ribosome; Cluster 2: positive regulation
974 of establishment of protein localization to telomere, association of TriC/CCT with target proteins during
975 biosynthesis, ATP-dependent protein folding chaperone; Cluster 3, tRNA-splicing ligase complex; Cluster
976 4: Myosin II filament, cell shape; Cluster 5: Nisch, Ube2i; Cluster 6: synthesis of active ubiquitin: roles of
977 E1 and E2 enzymes; Cluster 7: SHC-transforming protein 1 (SHC1) events in Erythroblastic Blast 2
978 (ERBB2) signaling, calcium-dependent protein kinase C activity, presynaptic cystosol. String protein-protein
979 interaction enrichment p-value < $1.0e^{-16}$. Ribosomal proteins found to interact with TDP-43 in other studies
980 are in bold within Cluster 1.(18, 91, 92)

981

982

983

984

985

986

987

988 proteins, lending further support to the notion that proteostasis-related processes are vulnerable
989 and dysregulated in mutant TDP-43 mice.(93)

990 There were 40 proteins that exhibited enhanced stabilization in Q331K versus WT cytosolic
991 lysates, although no cluster larger than 5 proteins was observed with STRING analyses and MCL
992 clustering. Cluster 1 and 2 each contain 5 proteins associated with smooth muscle contraction
993 and endocytosis, respectively (**Fig. S10G**). Interestingly, PISA detected four peptides derived
994 from ubiquitin (**Fig. 6E**) with sequence homology shared amongst ubiquitin C, ubiquitin B,
995 ubiquitin A-52 (Uba52) and Rps27a (**Supp. Table VI**). Uba52 and Rps27a are both ubiquitin-
996 ribosomal fusion proteins.(94) Therefore, despite downregulation of proteostasis-related
997 processes in Q331K mice at baseline, some compensatory mechanisms may be at play to
998 overcome these adverse effects.

999 **DISCUSSION**

1000 Herein, we show that expression of dysfunctional TDP-43 leads to deficits in multiple branches of
1001 the proteostasis network (**Fig. 7**). Proteostasis deficits occur independently of overt TDP-43
1002 overexpression, aggregation or mislocalization, which were not observed here or in prior reports
1003 describing this TDP-43 Q331K knock-in mouse model.(6, 44, 95) Analysis of our RNA-seq
1004 datasets comparing Q331K and WT mice without brain trauma (i.e., naïve or sham conditions)
1005 revealed downregulation of genes involved in protein folding, including multiple heat shock
1006 proteins and chaperones, as well as genes involved in the ubiquitin proteosome pathway, such
1007 as *Gid4* and *Spop*. Exon skipping of *Ube3c*, an RNA target of TDP-43 that encodes an E3 ubiquitin
1008 ligase, was also detected in brain lysates from Q331K mice. This gain of TDP-43 mis-splicing
1009 function was initially reported in TDP-43 mouse strains with endogenous mutations in the low
1010 complexity domain, including a Q331K variant.(82) Although changes in *Ube3c* expression levels
1011 were not detected by RNA-seq, AlphaFold and PyMol analyses predict that mis-splicing of *Ube3c*

could alter the structure of Ube3c near the ubiquitin-binding domain. Further, Fratta et al. reported that

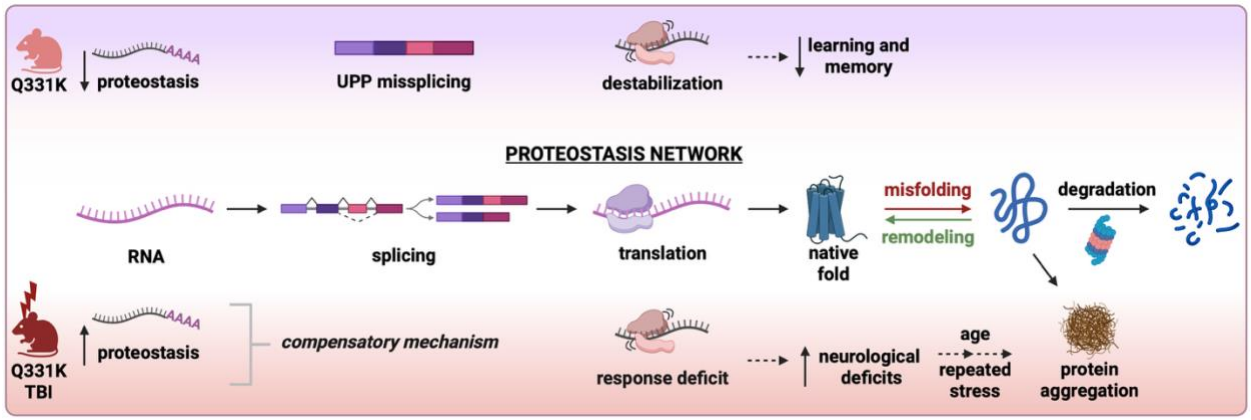

Figure 7. Proposed model for how the proteostasis network is affected by TDP-43 dysfunction. The proteostasis network is illustrated in the center of the diagram. Under baseline conditions (top), genes involved in proteostasis and the ubiquitin-proteasome pathway (UPP) are downregulated and mis-spliced in Q331K mouse brain relative to WT mice. In Q331K mouse brain lysates, ribosomal proteins are destabilized, which may compromise protein synthesis and thus contribute to the cognitive deficits observed in Q331K mice. In response to CNS challenge in form of a TBI (bottom), compensatory mechanisms appear to be activated in Q331K mice, including an upregulation of proteostasis-related genes at the RNA level. However, Q331K mice fail to mount a physiological response to TBI, as demonstrated by worse neurological deficits and delayed recovery after brain injury compared to their WT counterparts. We posit that destabilization of ribosomal proteins and chaperone complexes involved in proteostasis underly the enhanced neurological deficits exhibited by Q331K mice after TBI. Although Q331K mice ultimately recover from TBI, we predict that repeated CNS challenge as a function of aging will exacerbate the phenotypes uncovered herein, and could lead to neurodegeneration and pathological TDP-43 aggregation. Model figure generated with BioRender.

1033 about 15% of the exon skipping events identified in mutant TDP-43 mice occurred in genes within
1034 the ubiquitin proteosome pathway.(82) A decrease in proteosome-encoding transcripts early in
1035 life is a predictor of shortened lifespan in killifish, a vertebrate model used for aging studies.(96)
1036 Together, these observations support the notion that dysfunctional TDP-43 adversely affects the
1037 quality control arm of the proteostasis network, which in turn correlates with a decline in health
1038 and life-expectancy.
1039
1040 PISA, a novel approach for identifying alterations in biological complexes through thermostability
1041 measurements,(86, 87) further highlighted protein folding as a vulnerable component of the
1042 proteostasis network in Q331K mice, where multiple proteins within the essential molecular
1043 chaperone TRiC/CCT were found to be destabilized. Further, 20 out of 79 core ribosomal proteins
1044 were found to exhibit reduced thermal stability through our PISA analysis.(97) These data suggest
1045 that complexes formed by ribosomal proteins, namely ribosomes, could be affected by expression
1046 of dysfunctional TDP-43 in a manner that compromises this macromolecular complex (**Fig. 7**).
1047 TDP-43 has been shown to associate with ribosomal proteins through co-immunoprecipitation
1048 and proximity labeling experiments,(18, 47, 91, 92) and with actively translating ribosomes in
1049 cultured cells.(46, 47) Ribosomal proteins have also been detected within pathological TDP-43
1050 aggregates(47, 98) and in amyloid-positive aggregates within the aging brain.(96) In various
1051 contexts, TDP-43 expression can either repress or activate protein synthesis.(48, 49)
1052 Interestingly, the association of TDP-43 with translation-related factors can be modulated by the
1053 phase-separation behavior of TDP-43.(18) Proper phase separation of TDP-43 in vitro and in vivo
1054 requires residues 321-340, referred to as the conserved region (CR).(17-19) Deletion of the CR
1055 resulted in enhanced interactions between TDP-43 and translation factors together with
1056 heightened rates of global protein synthesis in vivo.(18) While the Q331K variant studied herein
1057 also reportedly disrupts TDP-43 phase separation,(17, 19) our polysome profiling data suggest
1058 that translation efficiency is reduced in Q331K mouse brain relative to WT brain. Therefore, there

1059 may be differential effects of the CR on translational regulation depending on how the TDP-43
1060 sequence is modified (i.e., deletion versus single point mutation). We note that PISA was
1061 performed on organelle-depleted brain lysates in this study, such that changes to nuclear and
1062 mitochondrial proteins would not have been captured in this analysis. Indeed, it will be interesting
1063 to extend PISA for analysis of other cellular compartments and organelles in future studies.
1064
1065 It remains to be determined precisely how expression of mutant Q331K in mice leads to reduced
1066 thermostability of ribosomal proteins. Disease-linked mutations may perturb interactions between
1067 TDP-43 and ribosomal proteins,(91) which could induce conformational changes within the
1068 ribosome (**Fig. 7**), other complexes that include ribosomal proteins and/or free ribosomal
1069 proteins.(99) Ribosomal protein stability could also be indirectly affected by mutant TDP-43
1070 expression. For example, altered proteostasis, activation of stress-response pathways and other
1071 stimuli can affect the post-translational modification status of ribosomal proteins, which may
1072 impact ribosome conformation and activity.(100) Intriguingly, ribosomal proteins underwent a shift
1073 toward enhanced stability in WT animals after TBI, possibly representing a mechanism that
1074 protects these proteins during cellular stress.(101) Although we do not observe changes in overall
1075 levels of ribosomal proteins in WT or Q331K mice, expression of mutant TDP-43 could influence
1076 the stoichiometry of ribosomal proteins, if not at the age of mice studied here (i.e., 16 weeks),
1077 potentially in older mice. The stoichiometry of ribosomes is reportedly compromised during aging,
1078 possibly a side-effect of impaired proteosome activity, which may lead to an accumulation of
1079 “orphan” ribosomal proteins that are prone to aggregate.(96, 101) TDP-43 dysfunction has also
1080 been linked to deficits in transporting mRNAs that encode ribosomal proteins(102) and in the
1081 stability of ribosome-encoding transcripts,(103) both of which could also impact ribosome integrity
1082 and protein translation.(48, 49) Deficiencies in protein synthesis may contribute to some cognitive
1083 deficits observed in Q331K mice,(44) including attenuated cue-induced freezing in the CCFC test
1084 in Q331K mice prior to surgery.(68) Although TBI is known to induce translational repression,

1085 upregulated expression of select proteins is thought to be important for mitigating the effects of
1086 trauma.(104) Our data support a model whereby Q331K mice are unable to mount a physiological
1087 response to TBI due to multiple deficits within the proteostasis network that likely include deficits
1088 in protein synthesis and folding (**Fig. 7**).
1089
1090 In addition to TBI,(13, 37-41) TDP-43 has been linked to other stress-related pathways in vitro(2-
1091 6, 11, 12) and in vivo.(15, 78). That TDP-43 undergoes a change in subcellular localization in
1092 response to a broad range of stressors suggests TDP-43 may serve as a general stress-sensor,
1093 a notion supported by our observation that TDP-43 re-distributes to the cytoplasm under
1094 conditions of sham surgery. Stress-induced subcellular re-distribution of TDP-43 is modulated by
1095 TDP-43 RNA-binding capacity and TDP-43 post-translational modification status, and this
1096 redistribution can coincide with mis-splicing signatures corresponding to TDP-43 loss of
1097 function.(3, 4, 7-9, 105) Here, we observe robust TBI-induced changes in subcellular TDP-43
1098 localization in both WT and Q331K mouse brain tissue, including a ring-like TDP-43 staining
1099 pattern that has not been widely reported. Changes in TDP-43 localization were most prominent
1100 in the hypothalamus and the amygdala, the latter region having been linked to behavioral
1101 dysfunction in human sporadic ALS.(106) *A priori*, we expected TBI-induced changes in TDP-43
1102 localization to coincide with splicing defects associated with TDP-43 loss-of-function.(4, 9, 82,
1103 105) However, the splicing patterns of known TDP-43 targets were primarily influenced by TDP-
1104 43 mutation and largely unaffected by TBI. It is possible that emerging reporters of TDP-43-
1105 mediated cryptic splicing could be more sensitive for detection of TDP-43 loss-of-function in cells
1106 with altered TDP-43 localization in our TBI model.(107)
1107
1108 The outcomes of our study lend support to the hypothesis that ALS pathogenesis occurs through
1109 a multistep process, where steps may represent genetic, environmental and/or behavioral risk
1110 factors.(34, 35) Notably, we detected a synergistic effect of TDP-43 mutation and TBI on gene

1111 expression profiles that are relevant to ALS pathogenesis. Indeed, there is substantial overlap in
1112 GSEA hallmark pathways in CNS tissues between Q331K TBI mice 24h post-TBI and human
1113 post-mortem ALS/FTLD-TDP cases,(45, 75) even though the Q331K TBI mice eventually recover,
1114 and the human cases represent end-stage disease. Our interpretation is that expression of mutant
1115 TDP-43 causes mice to become vulnerable to CNS challenge, resulting in dysregulation of key
1116 biological pathways that are also dysregulated during ALS/FTD pathogenesis. In Q331K mice,
1117 TBI-induced phenotypes that were observed 24h post-TBI, such as exaggerated neurological
1118 deficits (i.e., higher NSS), proteostasis-related gene upregulation, changes in *Ube3c* splicing and
1119 subcellular TDP-43 re-distribution, were largely restored to baseline levels 5-7 months post-TBI,
1120 consistent with this being a mild model of TBI.(43). Further, compensatory mechanisms, such as
1121 an upregulation of proteostasis-related genes, appear to be activated in Q331K mice (**Fig. 7**).
1122 Despite these protective measures, Q331K mice exhibited worse neurological outcomes in the
1123 acute phase post-TBI, indicating that stress-related pathways were vulnerable to dysfunctional
1124 TDP-43. This notion is further supported by a recent study demonstrating reduced stress granule
1125 formation in mutant TDP-43 mice exposed to hyperthermia.(15) We posit that repeated incidence
1126 of TBI and/or exposure to additional risk factors would lead to pathological and chronic
1127 degenerative phenotypes that persist months after the injury occurs (**Fig. 7**). Mathematical
1128 modeling of incidence data for human ALS cases with TDP-43 mutation indicated that disease
1129 pathogenesis may require up to five steps, where only one step is attributed to TDP-43
1130 mutation.(34, 35) In the case of sporadic ALS, six steps are predicted for disease pathogenesis.
1131 Accordingly, environmental and behavioral risk factors likely play a significant role in ALS
1132 pathogenesis.(32, 33) While the TDP-43 Q331K mutation represents one step in the current
1133 study, TDP-43 dysfunction can also manifest in the absence of genetic mutations. For example,
1134 altered post-translational and transcriptional forms of TDP-43 that have been detected in sporadic
1135 ALS cases have also been linked to TDP-43 dysfunction.(108, 109)
1136

1137 **Conclusions**

1138 Outcomes of this study demonstrate that expression of dysfunctional TDP-43 predisposes mice
1139 to worse neurological outcomes following brain trauma. Deficiencies in multiple branches of the
1140 proteostasis network likely contribute to this vulnerability of mutant TDP-43 mice to TBI (**Fig. 8**).
1141 Therefore, targeting the proteostasis network should be a viable therapeutic direction for treating
1142 TDP-43 proteinopathies. For example, proteostasis could be enhanced by mitigating protein
1143 misfolding and stress through activation of heat-shock proteins and chaperones.(110) TDP-43
1144 dysfunction can manifest through both genetic and non-genetic causes, where mutant TDP-43
1145 expression altered the physiological response to TBI herein. We predict that TDP-43 dysfunction
1146 will similarly affect cellular response and recovery pathways associated with other forms of CNS
1147 challenge.(15) Further, repeated and/or additional incidences of CNS challenge are expected to
1148 increase the likelihood of developing a TDP-43 proteinopathy such as ALS (**Fig. 8**).

1149

1150 **List of abbreviations**

Abbreviation	Description
AD	Alzheimer's disease
ALS	amyotrophic lateral sclerosis
BCA	bicinchoninic acid
BSA	bovine serum albumin
Calr	calreticulin
CCFC	cued and contextual fear conditioning
CR	conserved region
CTE	chronic traumatic encephalopathy
Dnajc5	DnaJ heat shock protein family (Hsp40) member 5
ER	endoplasmic reticulum
ES	enrichment score
FOV	field of view
FTD	frontotemporal dementia
FTLD	frontotemporal lobar degeneration
Gid4	glucose-induced degradation protein 4 homolog
GO	gene ontology

GOBP	gene Ontology biological process
GSEA	gene set enrichment analysis
GT	genotype
HECT	homologous to the E6-AP Carboxyl Terminus
Hspa4	heat shock 70 kDa protein 4
IACUC	Institutional Animal Care and Use Committee
IDR	intrinsically disordered region
INJ	Injury (i.e. sham or TBI)
Kcnip2	potassium voltage-gated channel interacting protein 2
LATE	limbic-predominant age-related TDP-43 encephalopathy
LC-MS/MS	liquid chromatography tandem mass spectrometry
Manf	mesencephalic astrocyte-derived neurotrophic factor
MCL	Markov Clustering
MSigDB	molecular signatures database
MTOR1	mammalian target of rapamycin complex 1
N/C	nuclear-to-cytoplasmic
NES	normalized enrichment score
NMDA	N-methyl-D-aspartate
NSS	neurological severity score
Pacrgl	parkin coregulated like
PCA	principal component analysis
Pdia3	protein disulfide isomerase family A, member 3
Pdia6	protein disulfide isomerase family A, member 6
PFA	paraformaldehyde
PISA	proteome integral solubility alteration
Ppp3ca	protein phosphatase 3 catalytic subunit alpha
pre-mRNA	pre-messenger RNA
PSM	peptide-spectrum match
PVDF	polyvinylidene fluoride
RNA-seq	bulk RNA-sequencing
RNP	ribonucleoprotein
Rplp1	large ribosomal subunit protein P1
Rps27a	ribosomal protein S27a
RT-PCR	Reverse transcription polymerase chain reaction
Slc6a6	solute carrier family 6 member 6
Sort1	Sortilin-1
Spop	speckle-type POZ protein
Ssr1	signal sequence receptor subunit 1
TAMC	Transgenic Animal Modeling Core

TBI	traumatic brain injury
TCP-1	cytosolic T-complex protein 1
TDP-43	TAR DNA-binding protein 43
TMT	tandem mass tag
TRiC/CCT	eukaryotic TCP-1 ring complex or chaperonin containing TCP-1
Tsn	translin
Uba52	ubiquitin A-52
Ube3c	ubiquitin protein ligase E3C
UPLC	UltraPerformance LC
WT	wild-type
Xbp1	active X-box binding protein 1
Xbp1s	spliced active X-box binding protein 1
Xbp1u	unspliced active X-box binding protein 1

Declarations

Ethics approval and consent to participate. Not applicable.

Consent for publication. Not applicable.

Availability of data and materials. Mass spectrometry proteomics data are available via ProteomeXchange with identifier PXD068825 and 10.6019/PXD068825.Submission of RNAseq dataset to GEO are in progress at the time of this manuscript submission.

Competing interests. The authors declare that they have no competing interests

Funding. This work was supported by CDMRP/DoD DOD/W81XWH-20-1-0271 (D.A.B and N.H), the Angel Fund for ALS Research (D.A.B and N.H.), NINDS R21NS139100 (D.A.B.), and the First Affiliated Hospital of Chongqing Medical University (J.Z.).

Authors' contributions. MSR performed all the mass spectrometry experiments and analyzed the resulting data, performed most of the RNAseq analyses and was a major contributor in writing and preparing the manuscript; **MFM** performed the TDP-43 localization analyses, contributed to the RNA-related analyses, and created multiple figures in the manuscript; **JZ** performed animal surgeries, performed the CCFC analyses, and acquired the confocal microscopy images; **KO** performed the RT-PCR analyses; **EAW** isolated RNA from mouse tissue and coordinated the

1168 RNA sequencing and provided some assistance in the analysis; **DC** maintained the mouse colony
1169 and assisted in the animal studies; **KS** assisted in the animal studies and performed
1170 immunofluorescence; **JB** performed the NSS tests and helped with surgeries; **HM** performed the
1171 AlphaFold analyses and contributed to the RT-PCR analyses; **MNA** performed the polysome
1172 profiling studies together with MSR; **FM** performed the PyMOL analyses and interpreted the
1173 results; **ART** and **SM** assisted in the CCFC study; **JAN** assisted with confocal microscopy; **NH**
1174 contributed to the experimental design for the TBI surgeries and analyzed the animal behavior
1175 data; **ODK** performed the tests of differential gene expression for the RNAseq data and was a
1176 major contributor to the omics analyses. **DAB** conceived and directed the project, analyzed data
1177 and wrote the manuscript with contributions from co-authors.

1178 **Acknowledgements.** We are grateful for services provided by UMass Chan core facilities
1179 including the Transgenic Animal Modeling Core, Mouse Behavioral Core, Mass Spectrometry
1180 Facility and Molecular Biology Core Labs. We thank Dr. Joel Richter for use of equipment and
1181 advice related to polysome profiling; Drs. Patrick Sullivan, Hemendra Vekaria, Myriam Heiman,
1182 Jack Humphrey, Sami Barmada, Christine Vande Velde and Clotilde Lagier-Tourenne and
1183 members of their labs for valuable advice; and current and former members of Bosco lab,
1184 especially Dr. Ozge Yildiz and Jonathan Jung for help on this project.

1185 **Authors' information.** Not applicable.

1186

1187

1188

1189

1190

1191

1192

1193

1194

1195

1196

1197 **Additional file 1. Supplemental Figures (Fig. S1 thru S11)**

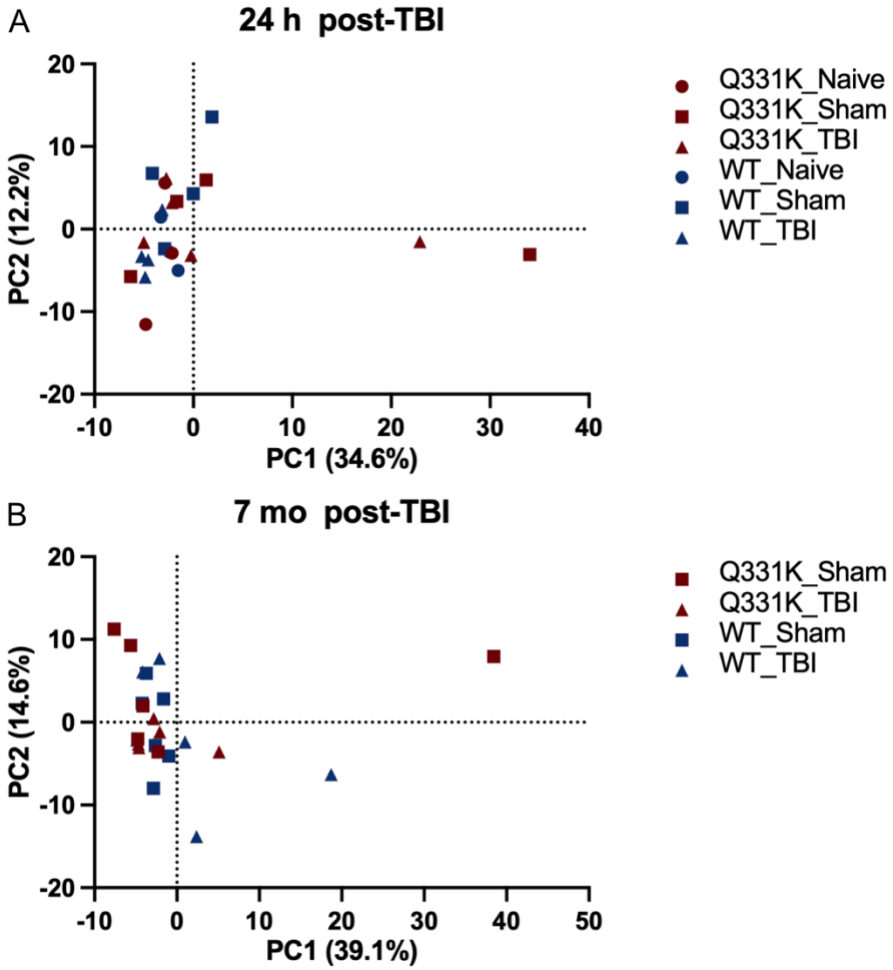

1198

1199 **Figure S1. Principal component analysis (PCA) identifies outliers in RNA-seq datasets.** PCA analysis using 1000

1200 genes with the highest de-trended variance for the 24 h post-TBI **(A)** and 7 mo post-TBI (**B**) datasets.

1201

1202

1203

1204

1205

1206

1207

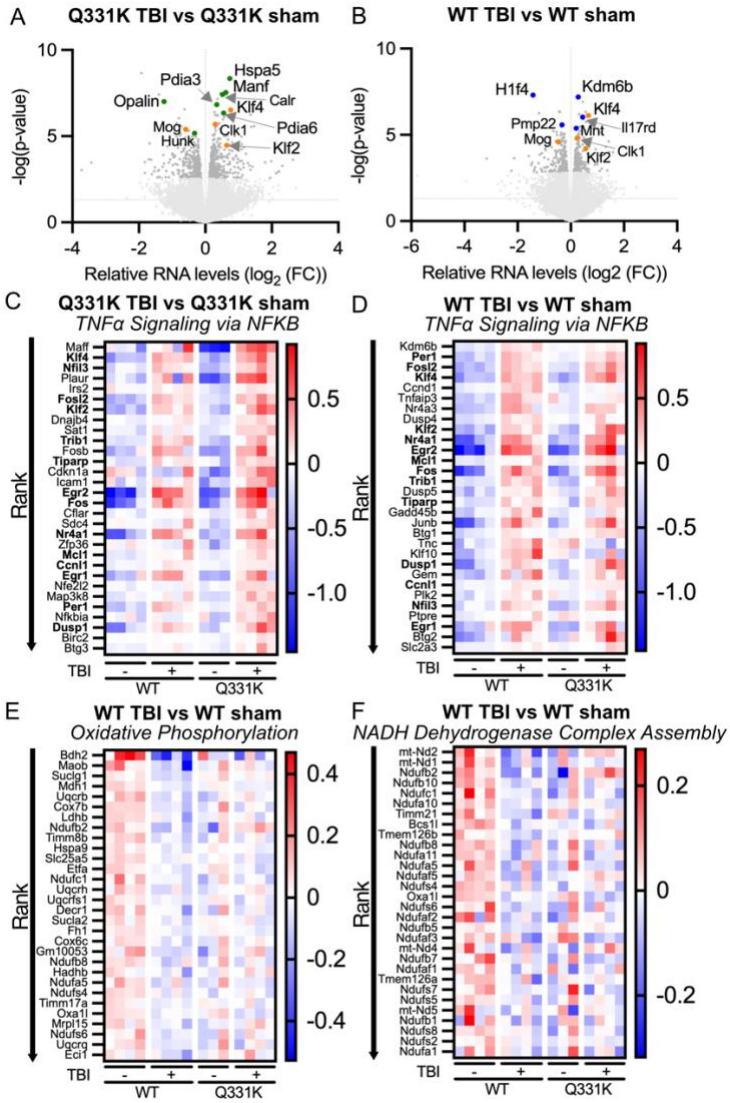

Figure S2. Overlapping and differential gene expression profiles in WT versus Q331K mice after TBI. (A) Volcano plot of transcriptional changes from RNAseq analyses for Q331K mice under conditions of TBI versus sham surgery. **(B)** Volcano plot of transcriptional changes from RNAseq analyses for WT mice under conditions of TBI versus sham surgery. **(A,B)** Hits with FDR <0.1 are shown in red. Orange dots highlight top gene hits (*Klf2*, *Klf4*, *Mog*, *Clk1*) resulting from TBI, irrespective of genotype. Blue dots denote top gene hits specifically in the WT TBI condition whereas green dots are top gene expression changes specifically in the Q331K TBI condition. **(C,D)** Heatmap showing the top 30 ranked genes in the top up-regulated pathway for hallmark gene set "TNFalpha signaling via NFKb" for Q331K TBI versus Q331K sham (C) and WT TBI versus WT sham (D). Fourteen genes (in bold) are significantly altered under "TNFalpha signaling via NFKb" for both the Q331K TBI and WT TBI conditions relative to their respective sham group. **(E,F)** Heatmap showing the top 30 ranked genes in the top down-regulated pathway in hallmark collection, "Oxidative Phosphorylation" (E), and Gene Ontology Biological Process collection, "NADH Dehydrogenase Complex Assembly" (F), for the WT TBI versus WT sham comparison. The $\log_2$(fold change) relative to the mean expression is shown for each sample.

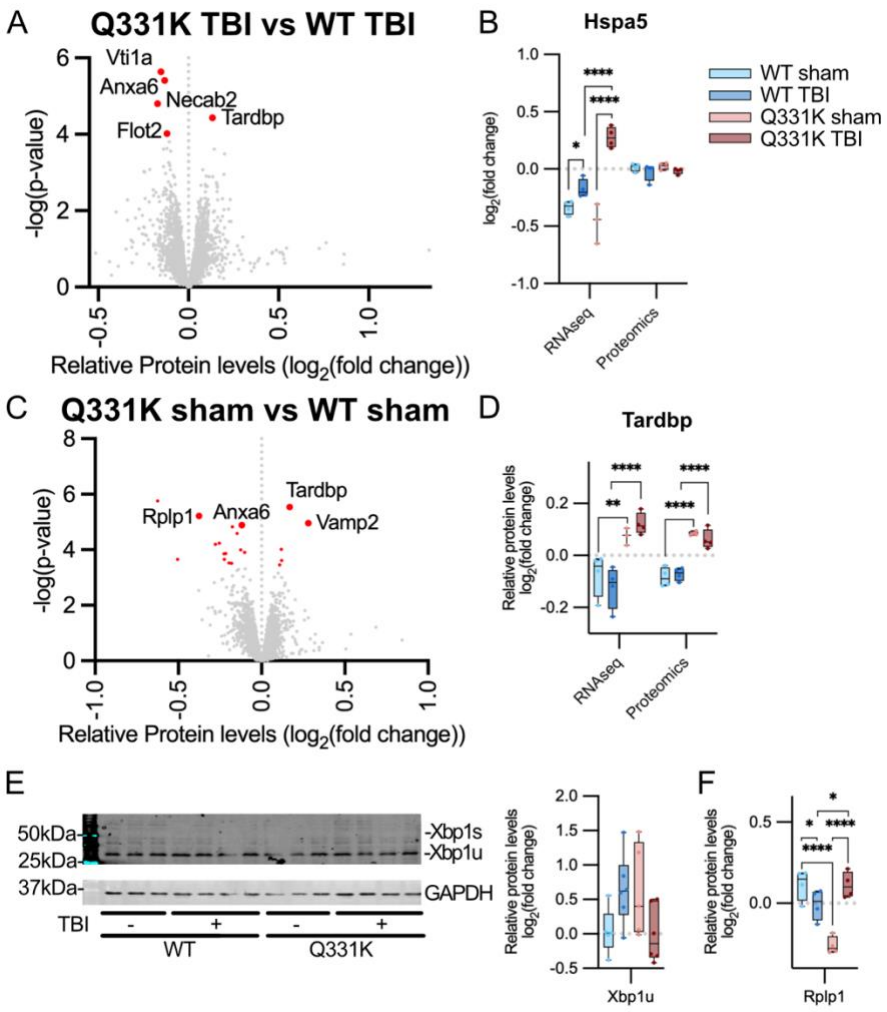

Figure S3. Proteomic analyses identify protein changes altered by TBI and mutant TDP-43 genotype. (A) Volcano plot showing relative protein level changes between Q331K TBI and WT TBI cohorts. Hits with FDR <0.1 are highlighted in red. **(B)** Hspa5 is unchanged at the protein level by quantitative proteomics. **(C)** Volcano plot showing relative protein level changes between Q331K sham and WT sham cohorts. Hits with FDR <0.1 are highlighted in red. **(D)** Tardbp is significantly elevated in Q331K mouse brain by transcriptomics and proteomics analyses. **(E)** Total levels of Xbp1 are unchanged and there is no detection of spliced Xbp1 by Western analysis. The expected molecular weight of spliced Xbp1 (Xbp1s) is 54 kDa and of unspliced Xbp1 (Xbp1u) is 29 kDa. Note, the band located at ~35 kDa is nonspecific. **(F)** Protein levels of Rplp1 as determined by quantitative proteomics. Nominal p-value = * <0.05; **<0.01, ****<0.0001.

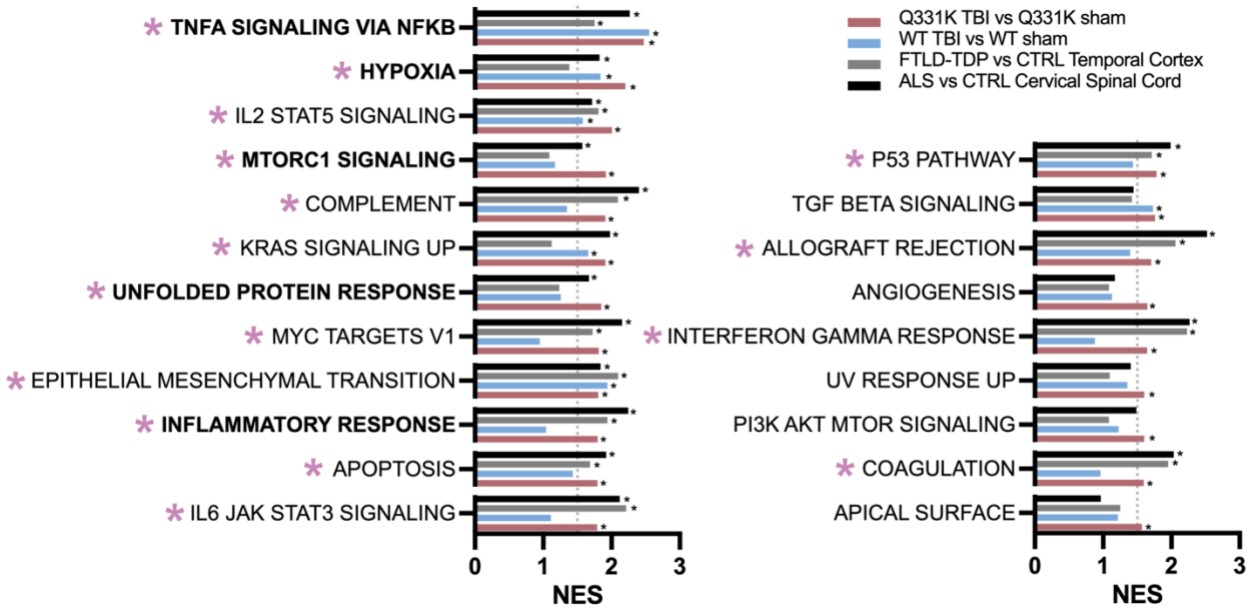

Figure S4. Comparison of published human ALS and FTLD post-mortem datasets with current TBI mouse study. Directional p-values were calculated from published datasets reported in Humphrey et al,(45) and Hasan et al (75) and subjected to GSEA using the hallmark database as described in methods for RNAseq. Asterisks to the right of the bars denote FDR<0.05 for the indicated comparison defined in the key. The dotted line indicates NES of 1.5. Pathways with a pink asterisk highlight those that are significant for the Q331K TBI versus Q331K sham comparison (pink bars), and at least one of the human datasets (grey and black bars). There are 16/21 pathways that meet this criterion, and only 5/21 pathways that are significant for the WT TBI versus WT sham comparison (blue bars) and at least one of the human datasets. Pathway names in bold are discussed in the main text.

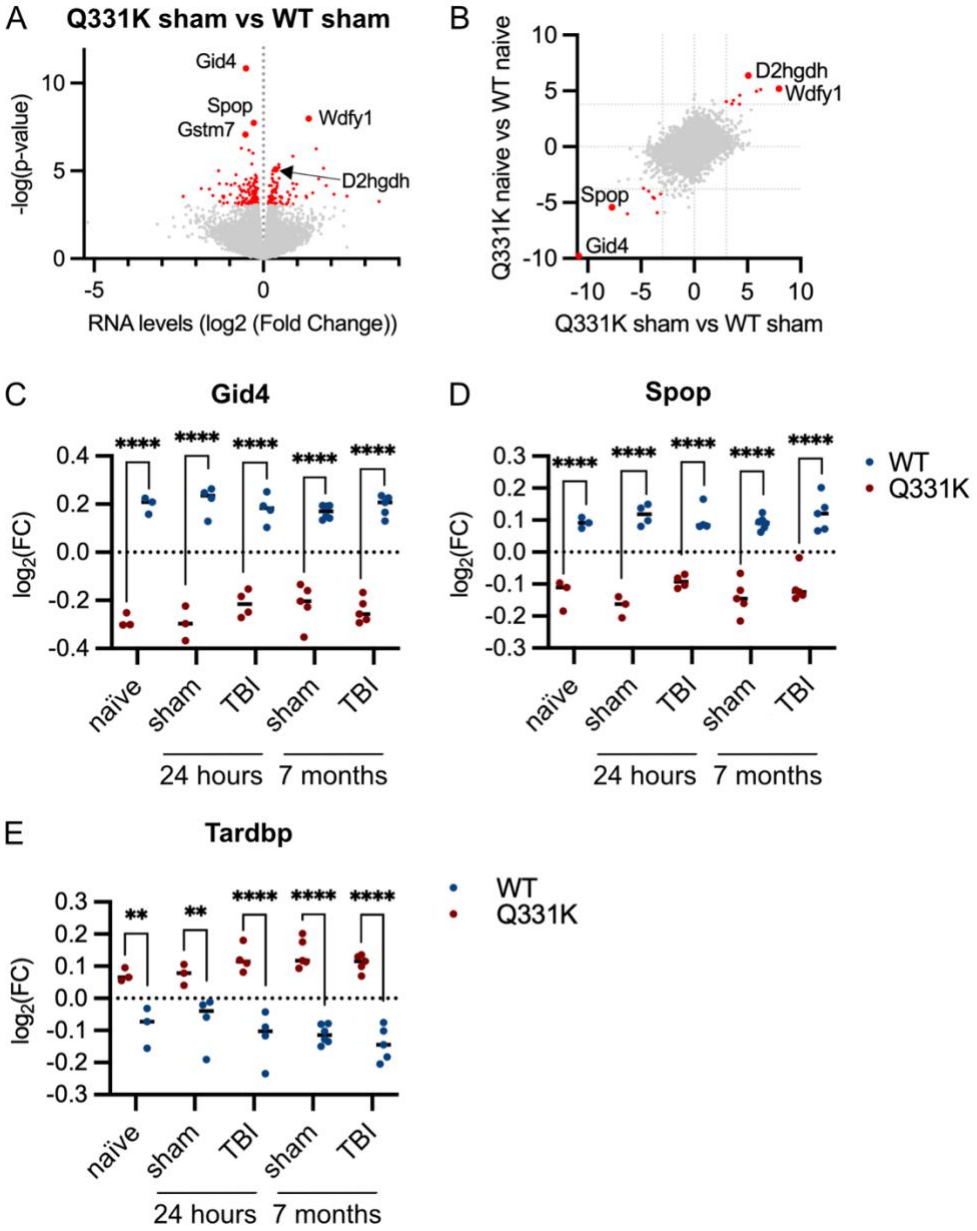

Figure S5. Omics analyses identify Q331K-specific changes to the transcriptome (A) Volcano plot with the significant up- and down-regulated transcripts in red for the Q331K sham versus WT sham comparison. **(B)** Directional p-value plot overlaying the Q331K sham versus WT sham datasets with the Q331K naive versus WT naive datasets to identify reproducible mutant TDP-43-specific changes, which are highlighted in red. Directional p-value = -log(p-value)*sign of $\log_2$(fold change) **(C-D)** Plots of the most significant Q331K-specific down-regulated genes, *Spop* and *Gid4*, which are both involved in the ubiquitin-proteosome pathway. **(E)** Elevated *Tardbp* is observed in all Q331K vs WT comparisons. For C-E, time post-surgery is indicated below. Nominal p-value = **<0.01, ****<0.0001.

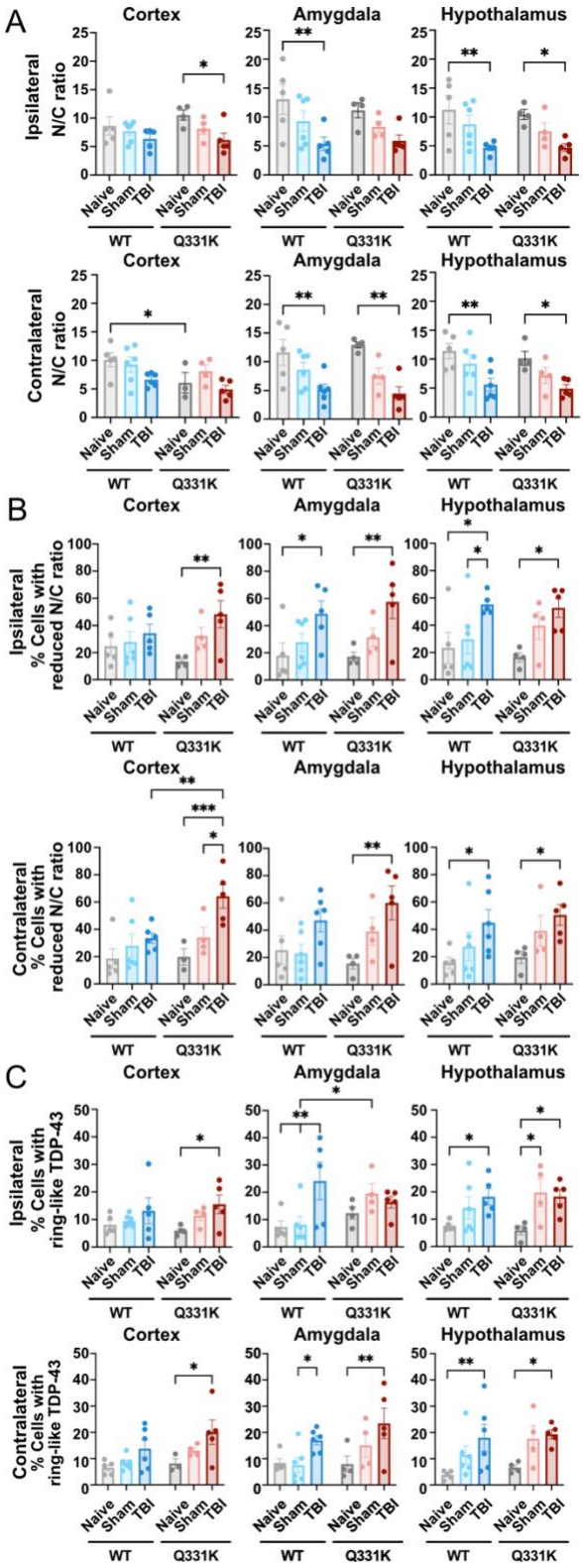

Figure S6. Changes in TDP-43 subcellular localization in mouse brain tissue 24h post-surgery. (A) Nuclear-to-cytoplasmic (N/C) ratio of TDP-43 signal in naïve mice or 24h post-surgery (sham or TBI) mice determined from immunofluorescence analysis of tissue sections from the cortex (left), amygdala (middle), and hypothalamus (right), either ipsilateral (top) or contralateral (bottom) to the TBI site. **(B)** Percent of cells that exhibit reduced TDP-43 N/C ratios in the tissues from (A). **(C)** Percent of cells that exhibit "ring-like" TDP-43 distribution in the tissues from (A). Each dot represents data from an individual mouse, with n=4-6 mice per cohort. Statistics was performed using two-way ANOVA followed by Tukey's multiple comparisons test between conditions. *p<0.05, **p<0.01, ***p<0.001, ****p<0.0001

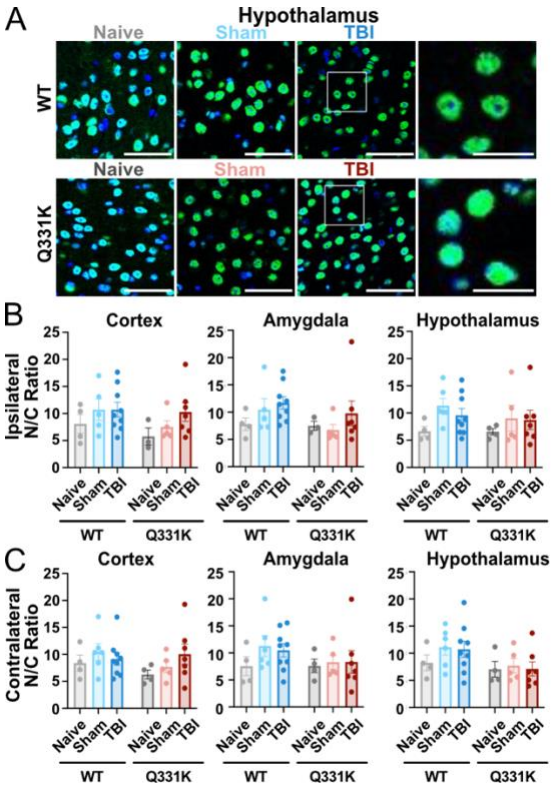

Figure S7. Lack of significant TDP-43 subcellular alteration in mouse brain tissue 5 months post-surgery. (A) Confocal immunofluorescence images of hypothalamus brain sections from WT and Q331K mice, either without surgery (naïve) or 5-months post-surgery (sham or TBI). Sections are stained for TDP-43 (green) and counterstained with DAPI (blue). Scale bars=20 um. **(B,C)** Quantification of the nuclear-to-cytoplasmic (N/C) ratio of TDP-43 signal in WT and Q331K mice 5-months post-surgery in the cortex, amygdala and hypothalamus, either ipsilateral (B) or contralateral with respect to the impact site. Each dot represents data from an individual mouse, with n=4-9 mice per cohort. Statistics was performed using two-way ANOVA followed by Tukey's multiple comparisons test between conditions.

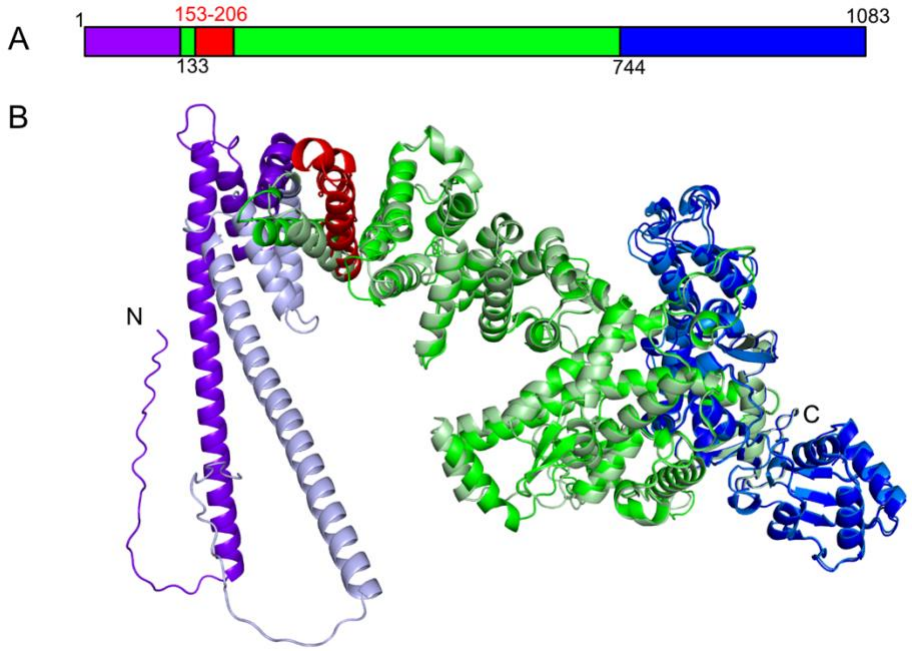

Figure S8. Structural analysis of TDP-43-relevant splice variants using AlphaFold and PyMOL. (A) Schematic representation of the ubiquitin-protein ligase E3C (Ube3c) protein highlighting distinct domains. Residue numbers are indicated at the start of each domain. The ubiquitin-binding domain (residues 1–132) is shown in purple, the second domain (residues 133–743) in green, and the catalytic Homologous to the E6-AP Carboxyl Terminus (HECT) domain (residues 744–1083) in blue. Residues corresponding to exon 6 (residues 153–206) are highlighted in red. **(B)** Overlay of AlphaFold-predicted structures for Ube3c containing exon 6 (domains in purple, green, and blue) with the predicted structures for Ube3c lacking exon 6 (domains in light purple, light green, and light blue). Structural alignments were performed in PyMOL, yielding an RMSD of 2.3 Å for alignment of only the ubiquitin-binding domain and an RMSD of 8.5 Å for the entire protein.

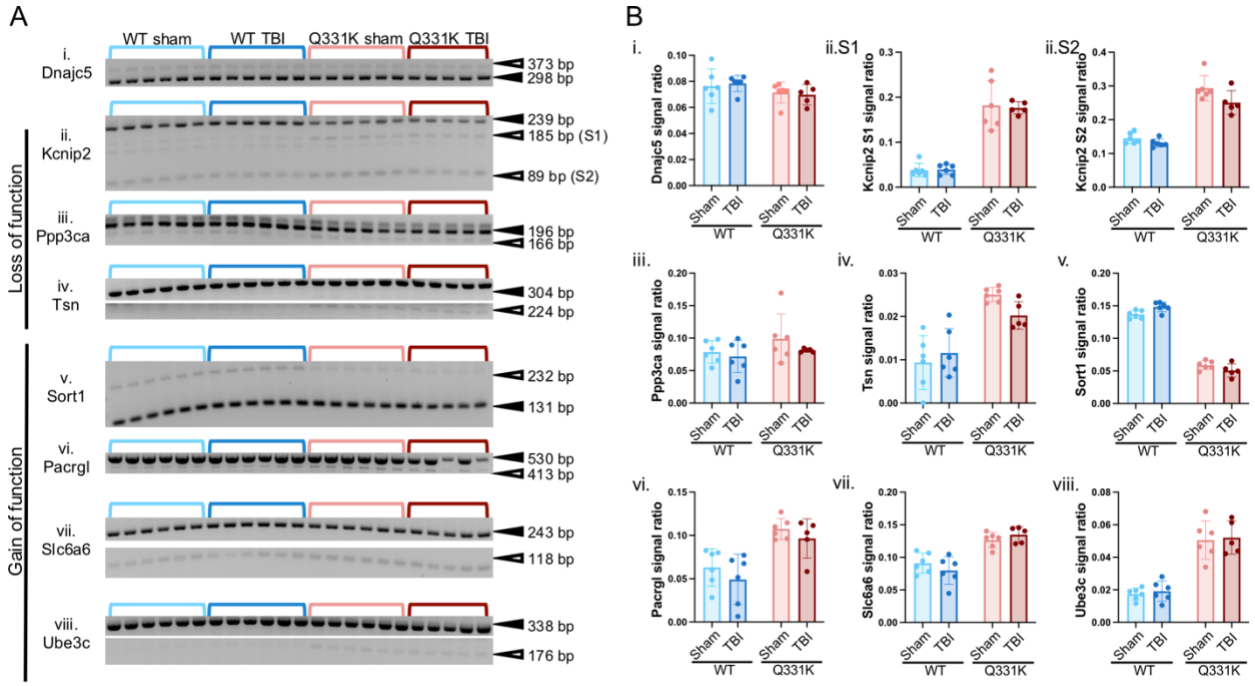

Figure S9. Alternative splicing targets of TDP-43 in WT and Q331K mice at 7 months post-injury. (A) Splice variants of known TDP-43 RNA targets (i-vi) detected by RT-PCR analysis in WT and Q331K mice 24h after either TBI or sham surgery. The PCR primers, exons of interest and references for the primers used in this study are shown in **Supp Table VI**. Splicing patterns that are consistent with TDP-43 loss of function or gain of function are indicated. Common and mis-spliced variants are denoted by, respectively, closed and open arrowheads with the corresponding size (bp=base pairs) of the PCR product. **(B)** Densitometry analysis of the gels in (A) was used to determine the ratio of the mis-spliced/common PCR product for each gene of interest. Each dot in the graph represents a separate mouse.

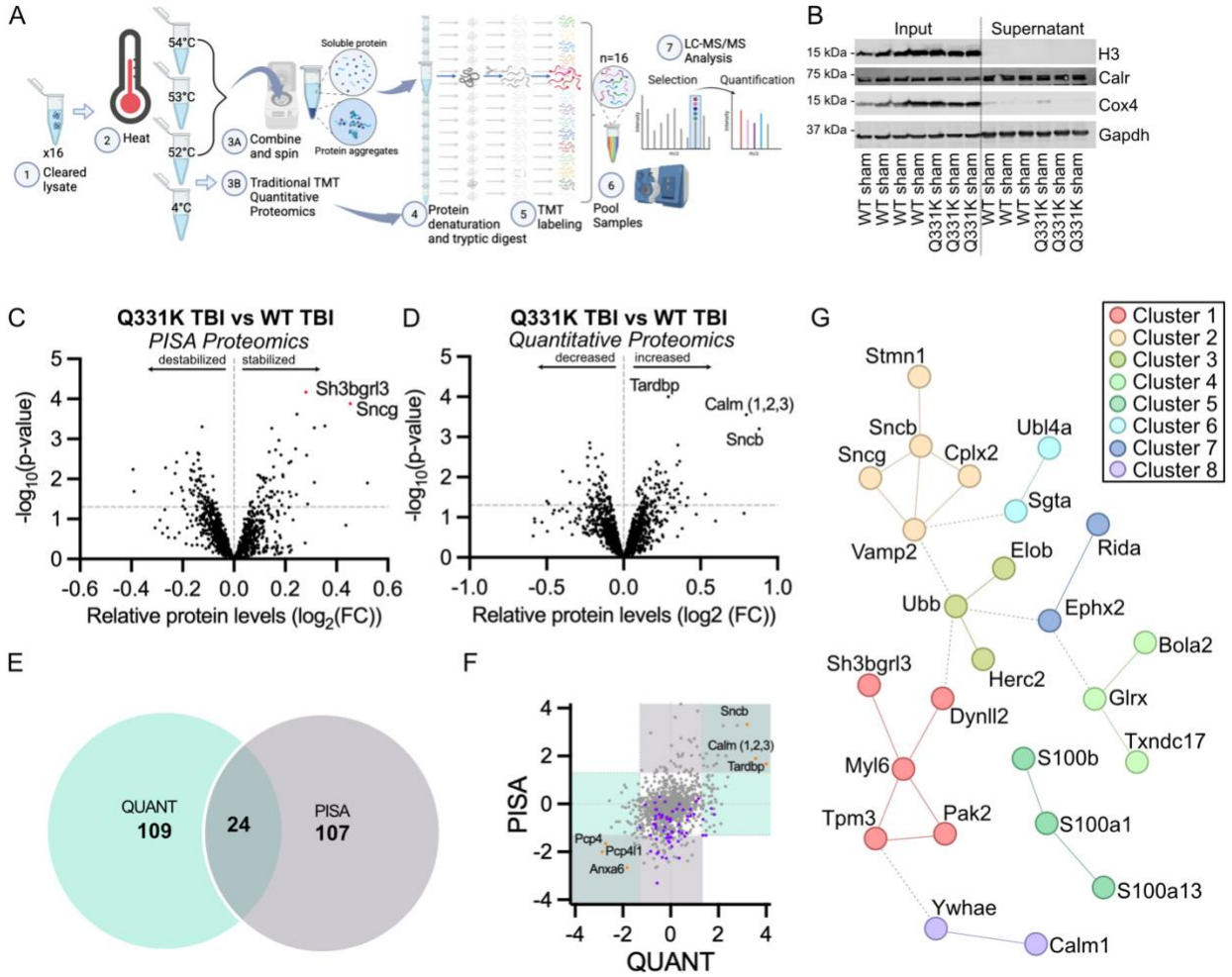

Figure S10. Quantitative proteomics of organelle-depleted cytoplasmic brain lysates. (**A**) PISA protocol for identifying proteins with altered thermostability between conditions: (1) Lysates are generated with mild, non-denaturing conditions and homogenization. Lysates are cleared by centrifugation. (2) Each sample is divided into four samples, where one is placed on ice for traditional quantitative proteomics and three are subjected to heat for protein denaturation. (3A) Aggregated protein is removed by centrifugation. (3B) The sample for traditional TMT quantitative proteomics remains on ice while samples for PISA are heated. (4) The soluble protein is digested with trypsin and labeled (5) with isobaric TMTpro-18plex tags. (6) Tagged samples are pooled, generating two sample sets (one from PISA and one from traditional quantitative proteomics) and subjected to mass spectrometry for quantification (7). Created with biorender.com. (**B**) Western analyses of organelle depleted supernatant (supernatant) compared to the whole brain sample input (input). (**C-D**) Volcano plot of protein changes identified by traditional quantitative proteomics (**C**) and PISA (**D**) for Q331K TBI versus WT TBI conditions. (**E**) Overlapping hits between quantitative proteomics and PISA are assessed to distinguish protein level changes from thermostability changes. (**F**) Directional p-value plot of Q331K TBI versus WT TBI for PISA and QUANT (quantitative proteomics). Purple dots indicate ribosomal proteins.

1355 Orange dots are highlighting top hits found in both PISA and QUANT. (**G**) Clustering using the Markov Cluster Algorithm
1356 for “Q331K All” versus “WT All” (defined in Figure 7 legend) for the stabilized proteins passing FDR adjustment (FDR
1357 <0.1). Only proteins identified as part of a cluster are shown. Cluster 1: Smooth Muscle Contraction; Cluster 2: Synaptic
1358 vesicle endocytosis, Synaptobrevin 2-SNAP-25-syntaxin-1a-complexin II complex; Cluster 3: Inactivation of
1359 Granulocyte colony-stimulating factor (G-CSF) signaling; Cluster 4: Protein-disulfide reductase nicotinamide adenine
1360 dinucleotide phosphate (NAD(P)) activity; Cluster 5: S-100/Intestinal calcium-binding protein (ICaBP) type calcium
1361 binding domain; Cluster 6: ER membrane insertion complex; Cluster 7: Epoxide hydrolase 2 (Ephx2), reactive
1362 intermediate imine deaminase A (Rida); Cluster 8: Negative regulation of calcium ion export across plasma membrane.
1363 Protein-protein interaction enrichment p-value = $2.94e^{-06}$.
1364
1365
1366

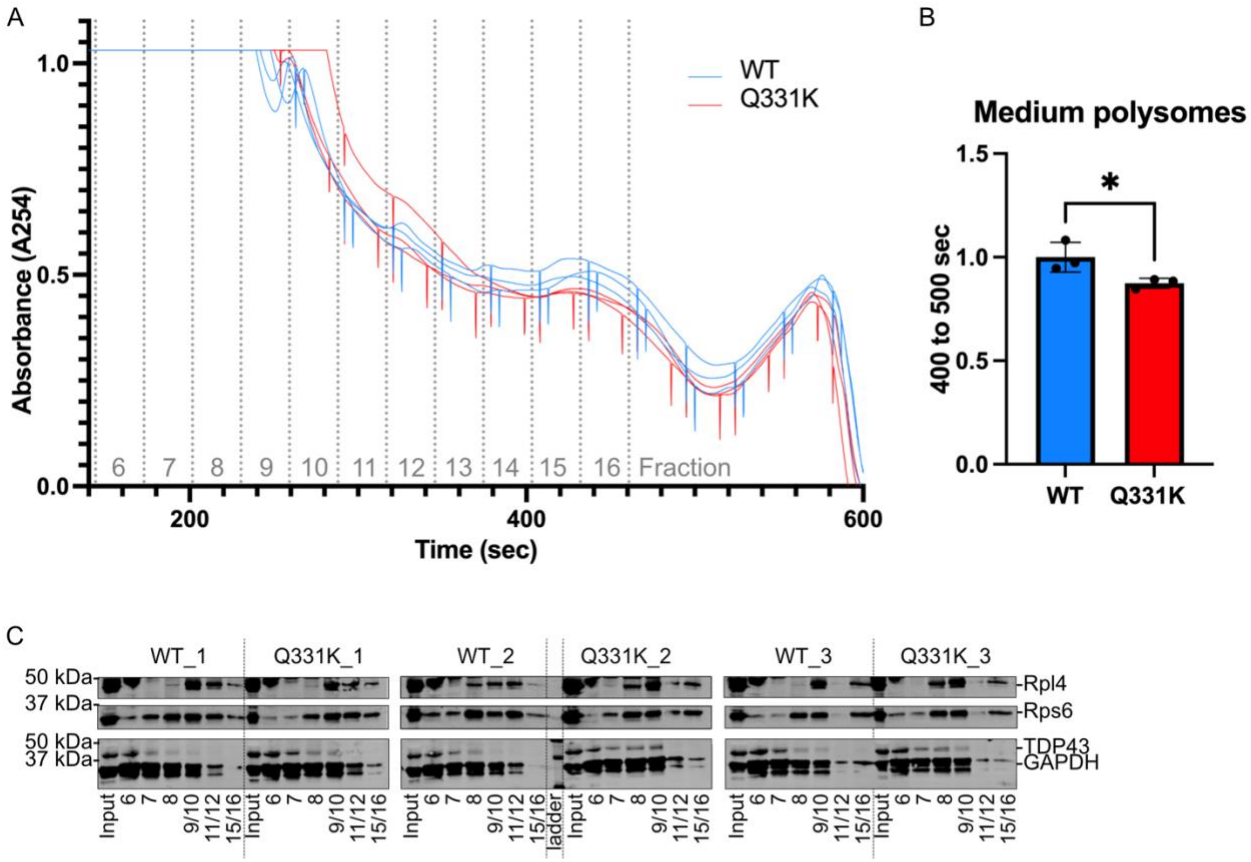

D

Sample	28S/18S	RQN
WT_1	1.3	9
Q331K_1	1.2	9.2
WT_2	1.3	9
Q331K_2	1.4	9.1
WT_3	1.0	7.9
Q331K_3	0.9	6.0

Figure S11. Polysome profiling of cytoplasmic fractions confirm the presence of intact ribosomes. **(A)** Graph of sucrose gradient fractions post-ultracentrifugation. The prominent peaks are at fractions 9/10, fractions 11/12, and fractions 15/16. **(B)** The area under the curve was calculated for all samples at 400 sec to 500 sec to estimate relative amount of medium polysomes, as this was the only ribosomal peak consistently observed in all samples. * = p-value <0.05. **(C)** Western analyses of the protein precipitated fractions of the polysome profile shown in A. Numbers indicate specific fractions analyzed. **(D)** Fragment analysis of RNA isolated from cytoplasmic fractions for each sample subjected to polysome profiling using the Agilent Fragment Analyzer.

1379 **Additional file 2. FIJI Macro for Per FOV N/C Analysis**. Macro script to be used in
1380 FIJI/ImageJ to complete TDP-43 localization analysis on a per FOV level. DAPI signal is used to
1381 define and separate the nuclear and non-nuclear regions where TDP-43 fluorescent signal is
1382 measured to determine the N/C ratio.
1383
1384 **Additional file 3. CellProfiler Pipeline for Per Cell N/C Ratio and Ring-like Analysis.**
1385 CellProfiler Pipeline used for per cell analyses of TDP-43 fluorescent signal including N/C ratio
1386 and ring-like TDP-43 signal. DAPI signal is used to identify individual cells, as well as define
1387 nuclear and cytoplasmic regions for N/C ratio analyses. For ring-like analysis, the nuclear region
1388 is binned into 3 rings to report on distribution of TDP-43 signal.
1389
1390 **Additional file 4, Supp. Table I. Statistical output of RNAseq analyses**. For all comparisons,
1391 logFC refers to log2(fold change), PValue refers to nominal p-value, and FDR refers to adjusted
1392 p-value. Nominal p-values <0.05 are indicated in orange and FDR < 0.1 in red. (**IA**) Statistical
1393 analyses for the 4 mo old mouse cohorts including the 24 h post-surgery (TBI and sham) and
1394 naïve groups. (**IB**) Statistical analyses for the 7 mo post-surgery cohorts.
1395
1396 **Additional file 5, Supp.Table II. GSEA Pathway analyses for all comparisons from the**
1397 **RNAseq analysis**. All pathway hits that passed the cutoff criteria (NES > 1.5, FDR > 0.05) are
1398 listed. Each tab is a unique group comparison. In each tab, the top upregulated pathways are
1399 beneath the purple-shaded header on the left, while the top downregulated pathways are beneath
1400 the blue-shaded header on the right. Results of hallmark and GOBP are shown. (**IIA**) List of
1401 abbreviations used in the file. (**IIB-E**) Pathway hits for the 24h-post surgery (TBI and sham). (**IIF**)
1402 Pathway hits for Q331K naïve mice relative to WT naïve mice at 4 months of age. (**IIG-IIJ**) Detailed
1403 gene lists for the top pathway hits for the 24h group comparisons. (**IIK-IIN**) Pathway hits for each
1404 group comparison at 7 mo post-surgery.
1405
1406 **Additional file 6, Supp. Table III. Statistical analyses of whole brain quantitative proteomics**
1407 **from Q331K and WT mice with surgery**. Unadjusted p-values ≤ 0.05 are highlighted red
1408 (columns H-K). Adjusted p-values ≤ 0.1 are highlighted in red (columns L-O). Coef. refers to
1409 Log_2(fold change); P.value indicates nominal p-value; P.value.adj. represents adjusted p-value
1410 (FDR).
1411
1412 **Additional file 7, Supp. Table IV. Overlap of published omics datasets with the current**
1413 **study.** Includes all identified proteome and transcriptome level changes in Q331K relative to WT
1414 mice from the current study. Columns B-D refer to datasets in the present study. RNAseq_Sham
1415 refers to the Q331K sham versus WT sham comparison. RNAseq_Naive refers to Q331K naïve
1416 versus WT naïve at 4 months of age. Proteomics_Sham refers to Q331K sham versus WT sham
1417 whole brain proteomics. Columns E/F refer to results published by White et al.(44).
1418
1419 **Additional file 8, Supp. Table V. RT-PCR primers.** Sequence information for primers that were
1420 used to identify alternative splicing for targets of TDP-43 in **Figures 5** and **S8**.
1421
1422 **Additional file 9, Supp. Table VI. Significant outcomes from quantitative proteomics on**
1423 **organelle-depleted cytoplasmic brain lysates.** (**VIIA**) PISA quantitative proteomics results.
1424 (**VIIB**) Traditional quantitative proteomics results (i.e. not exposed to heat). Unadjusted p-values
1425 ≤ 0.05 are highlighted red (columns K-Q). Adjusted p-values ≤ 0.1 are highlighted in red (columns
1426 R-X). Coef. refers to Log_2(fold change); P.value indicates nominal p-value; P.value.adj.
1427 represents adjusted p-value (FDR).
1428

1429 **Additional file 10, Supp. Table VII. GSEA pathway analyses of quantitative proteomics**
1430 **outcomes for organelle-depleted cytoplasmic brain lysates.** All pathway hits that passed the
1431 cutoff criteria (NES > 1.5, FDR > 0.05) are listed. Each tab is a unique group comparison. In each
1432 tab, the top upregulated pathways are beneath the purple-shaded header on the left, while the
1433 top downregulated pathways are beneath the blue-shaded header on the right. Results of
1434 hallmark and GOBP are shown. (**VIIIA-D**) Pathway hits for samples processed using PISA. (**VIIIE-**
1435 **H**) Pathway hits from the traditional quantitative proteomics anlaysis.
1436

1437 **References**

1438 1. Buratti E, Baralle FE. Multiple roles of TDP-43 in gene expression, splicing regulation,
1439 and human disease. Front Biosci. 2008;13:867-78.
1440 2. Dewey CM, Cenik B, Sephton CF, Dries DR, Mayer P, 3rd, Good SK, et al. TDP-43 is
1441 directed to stress granules by sorbitol, a novel physiological osmotic and oxidative stressor.
1442 Molecular and cellular biology. 2010.
1443 3. Duan L, Zaepfel BL, Aksenova V, Dasso M, Rothstein JD, Kalab P, et al. Nuclear RNA
1444 binding regulates TDP-43 nuclear localization and passive nuclear export. Cell Rep.
1445 2022;40(3):111106.
1446 4. Klim JR, Williams LA, Limone F, Guerra San Juan I, Davis-Dusenbery BN, Mordes DA,
1447 et al. ALS-implicated protein TDP-43 sustains levels of STMN2, a mediator of motor neuron
1448 growth and repair. Nat Neurosci. 2019;22(2):167-79.
1449 5. Tischbein M, Baron DM, Lin YC, Gall KV, Landers JE, Fallini C, et al. The RNA-binding
1450 protein FUS/TLS undergoes calcium-mediated nuclear egress during excitotoxic stress and is
1451 required for GRIA2 mRNA processing. J Biol Chem. 2019;294(26):10194-210.
1452 6. Weskamp K, Tank EM, Miguez R, McBride JP, Gomez NB, White M, et al. Shortened
1453 TDP43 isoforms upregulated by neuronal hyperactivity drive TDP43 pathology in ALS. J Clin
1454 Invest. 2020;130(3):1139-55.
1455 7. Perez-Berlanga M, Wiersma VI, Zbinden A, De Vos L, Wagner U, Foglieni C, et al. Loss
1456 of TDP-43 oligomerization or RNA binding elicits distinct aggregation patterns. EMBO J.
1457 2023;42(17):e111719.
1458 8. Zhang S, Vazquez-Sanchez S, Lu S, Baughn MW, Lim J, Oung S, et al. Acetylation of
1459 lysine 82 initiates TDP-43 nuclear loss of function by disrupting its nuclear import. bioRxiv.
1460 2024:2024.09.04.611121.
1461 9. Necarsulmer JC, Simon JM, Evangelista BA, Chen Y, Tian X, Nafees S, et al. RNA-
1462 binding deficient TDP-43 drives cognitive decline in a mouse model of TDP-43 proteinopathy.
1463 Elife. 2023;12.
1464 10. Dos Passos PM, Hemamali EH, Mamede LD, Hayes LR, Ayala YM. RNA-mediated
1465 ribonucleoprotein assembly controls TDP-43 nuclear retention. PLoS Biol.
1466 2024;22(2):e3002527.
1467 11. Liu-Yesucevitz L, Bilgutay A, Zhang YJ, Vanderwyde T, Citro A, Mehta T, et al. Tar DNA
1468 binding protein-43 (TDP-43) associates with stress granules: analysis of cultured cells and
1469 pathological brain tissue. PloS one. 2010;5(10):e13250.
1470 12. McDonald KK, Aulas A, Destroismaisons L, Pickles S, Beleac E, Camu W, et al. TAR
1471 DNA-binding protein 43 (TDP-43) regulates stress granule dynamics via differential regulation of
1472 G3BP and TIA-1. Human molecular genetics. 2011.
1473 13. Anderson EN, Gochenaur L, Singh A, Grant R, Patel K, Watkins S, et al. Traumatic
1474 injury induces Stress Granule Formation and enhances Motor Dysfunctions in ALS/FTD Models.
1475 Human molecular genetics. 2018.

1476 14. Alami NH, Smith RB, Carrasco MA, Williams LA, Winborn CS, Han SSW, et al. Axonal
1477 transport of TDP-43 mRNA granules is impaired by ALS-causing mutations. Neuron.
1478 2014;81(3):536-43.
1479 15. Dubinski A, Gagne M, Peyrard S, Gordon D, Talbot K, Vande Velde C. Stress granule
1480 assembly in vivo is deficient in the CNS of mutant TDP-43 ALS mice. Human molecular
1481 genetics. 2023;32(2):319-32.
1482 16. Gopal PP, Nirschl JJ, Klinman E, Holzbaur EL. Amyotrophic lateral sclerosis-linked
1483 mutations increase the viscosity of liquid-like TDP-43 RNP granules in neurons. Proc Natl Acad
1484 Sci U S A. 2017;114(12):E2466-E75.
1485 17. Conicella AE, Zerze GH, Mittal J, Fawzi NL. ALS Mutations Disrupt Phase Separation
1486 Mediated by alpha-Helical Structure in the TDP-43 Low-Complexity C-Terminal Domain.
1487 Structure. 2016;24(9):1537-49.
1488 18. Gao J, Wang L, Ren X, Dunn JR, Peters A, Miyagi M, et al. Translational regulation in
1489 the brain by TDP-43 phase separation. J Cell Biol. 2021;220(10).
1490 19. Hallegger M, Chakrabarti AM, Lee FCY, Lee BL, Amalietti AG, Odeh HM, et al. TDP-43
1491 condensation properties specify its RNA-binding and regulatory repertoire. Cell.
1492 2021;184(18):4680-96 e22.
1493 20. Grese ZR, Bastos AC, Mamede LD, French RL, Miller TM, Ayala YM. Specific RNA
1494 interactions promote TDP-43 multivalent phase separation and maintain liquid properties.
1495 EMBO Rep. 2021;22(12):e53632.
1496 21. de Boer EMJ, Orie VK, Williams T, Baker MR, De Oliveira HM, Polvikoski T, et al. TDP-
1497 43 proteinopathies: a new wave of neurodegenerative diseases. J Neurol Neurosurg Psychiatry.
1498 2020;92(1):86-95.
1499 22. Arai T, Hasegawa M, Akiyama H, Ikeda K, Nonaka T, Mori H, et al. TDP-43 is a
1500 component of ubiquitin-positive tau-negative inclusions in frontotemporal lobar degeneration
1501 and amyotrophic lateral sclerosis. Biochem Biophys Res Commun. 2006;351(3):602-11.
1502 23. Neumann M, Sampathu DM, Kwong LK, Truax AC, Micsenyi MC, Chou TT, et al.
1503 Ubiquitinated TDP-43 in frontotemporal lobar degeneration and amyotrophic lateral sclerosis.
1504 Science. 2006;314(5796):130-3.
1505 24. Amador-Ortiz C, Lin WL, Ahmed Z, Personett D, Davies P, Duara R, et al. TDP-43
1506 immunoreactivity in hippocampal sclerosis and Alzheimer's disease. Ann Neurol.
1507 2007;61(5):435-45.
1508 25. Nelson PT, Dickson DW, Trojanowski JQ, Jack CR, Boyle PA, Arfanakis K, et al. Limbic-
1509 predominant age-related TDP-43 encephalopathy (LATE): consensus working group report.
1510 Brain. 2019;142(6):1503-27.
1511 26. McKee AC, Gavett BE, Stern RA, Nowinski CJ, Cantu RC, Kowall NW, et al. TDP-43
1512 proteinopathy and motor neuron disease in chronic traumatic encephalopathy. J Neuropathol
1513 Exp Neurol. 2010;69(9):918-29.
1514 27. Brown AL, Wilkins OG, Keuss MJ, Hill SE, Zanovello M, Lee WC, et al. TDP-43 loss and
1515 ALS-risk SNPs drive mis-splicing and depletion of UNC13A. Nature. 2022;603(7899):131-7.
1516 28. Estades Ayuso V, Pickles S, Todd T, Yue M, Jansen-West K, Song Y, et al. TDP-43-
1517 regulated cryptic RNAs accumulate in Alzheimer's disease brains. Mol Neurodegener.
1518 2023;18(1):57.
1519 29. Ling JP, Pletnikova O, Troncoso JC, Wong PC. TDP-43 repression of nonconserved
1520 cryptic exons is compromised in ALS-FTD. Science. 2015;349(6248):650-5.
1521 30. Ma XR, Prudencio M, Koike Y, Vatsavayai SC, Kim G, Harbinski F, et al. TDP-43
1522 represses cryptic exon inclusion in the FTD-ALS gene UNC13A. Nature. 2022;603(7899):124-
1523 30.
1524 31. Melamed Z, Lopez-Erauskin J, Baughn MW, Zhang O, Drenner K, Sun Y, et al.
1525 Premature polyadenylation-mediated loss of stathmin-2 is a hallmark of TDP-43-dependent
1526 neurodegeneration. Nat Neurosci. 2019;22(2):180-90.

1527 32. Al-Chalabi A, Hardiman O. The epidemiology of ALS: a conspiracy of genes,
1528 environment and time. Nat Rev Neurol. 2013;9(11):617-28.
1529 33. Goutman SA, Savelieff MG, Jang DG, Hur J, Feldman EL. The amyotrophic lateral
1530 sclerosis exposome: recent advances and future directions. Nat Rev Neurol. 2023;19(10):617-
1531 34.
1532 34. Chio A, Mazzini L, D'Alfonso S, Corrado L, Canosa A, Moglia C, et al. The multistep
1533 hypothesis of ALS revisited: The role of genetic mutations. Neurology. 2018;91(7):e635-e42.
1534 35. Al-Chalabi A, Calvo A, Chio A, Colville S, Ellis CM, Hardiman O, et al. Analysis of
1535 amyotrophic lateral sclerosis as a multistep process: a population-based modelling study.
1536 Lancet Neurol. 2014;13(11):1108-13.
1537 36. Barker S, Paul BD, Pieper AA. Increased Risk of Aging-Related Neurodegenerative
1538 Disease after Traumatic Brain Injury. Biomedicines. 2023;11(4).
1539 37. Heyburn L, Sajja V, Long JB. The Role of TDP-43 in Military-Relevant TBI and Chronic
1540 Neurodegeneration. Front Neurol. 2019;10:680.
1541 38. Jankovic T, Dolenec P, Rajic Bumber J, Grzeta N, Kriz J, Zupan G, et al. Differential
1542 Expression Patterns of TDP-43 in Single Moderate versus Repetitive Mild Traumatic Brain Injury
1543 in Mice. Int J Mol Sci. 2021;22(22).
1544 39. Kahriman A, Bouley J, Smith TW, Bosco DA, Woerman AL, Henninger N. Mouse closed
1545 head traumatic brain injury replicates the histological tau pathology pattern of human disease:
1546 characterization of a novel model and systematic review of the literature. Acta Neuropathol
1547 Commun. 2021;9(1):118.
1548 40. Kahriman A, Bouley J, Tuncali I, Dogan EO, Pereira M, Luu T, et al. Repeated mild
1549 traumatic brain injury triggers pathology in asymptomatic C9ORF72 transgenic mice. Brain.
1550 2023;146(12):5139-52.
1551 41. Wiesner D, Tar L, Linkus B, Chandrasekar A, Olde Heuvel F, Dupuis L, et al. Reversible
1552 induction of TDP-43 granules in cortical neurons after traumatic injury. Exp Neurol. 2018;299(Pt
1553 A):15-25.
1554 42. Stein TD, Alvarez VE, McKee AC. Chronic traumatic encephalopathy: a spectrum of
1555 neuropathological changes following repetitive brain trauma in athletes and military personnel.
1556 Alzheimers Res Ther. 2014;6(1):4.
1557 43. Henninger N, Bouley J, Sikoglu EM, An J, Moore CM, King JA, et al. Attenuated
1558 traumatic axonal injury and improved functional outcome after traumatic brain injury in mice
1559 lacking Sarm1. Brain. 2016;139(Pt 4):1094-105.
1560 44. White MA, Kim E, Duffy A, Adalbert R, Phillips BU, Peters OM, et al. TDP-43 gains
1561 function due to perturbed autoregulation in a Tardbp knock-in mouse model of ALS-FTD. Nat
1562 Neurosci. 2018;21(4):552-63.
1563 45. Humphrey J, Venkatesh S, Hasan R, Herb JT, de Paiva Lopes K, Kucukali F, et al.
1564 Integrative transcriptomic analysis of the amyotrophic lateral sclerosis spinal cord implicates
1565 glial activation and suggests new risk genes. Nat Neurosci. 2023;26(1):150-62.
1566 46. Neelagandan N, Gonnella G, Dang S, Janiesch PC, Miller KK, Kuchler K, et al. TDP-43
1567 enhances translation of specific mRNAs linked to neurodegenerative disease. Nucleic Acids
1568 Res. 2019;47(1):341-61.
1569 47. Russo A, Scardigli R, La Regina F, Murray ME, Romano N, Dickson DW, et al.
1570 Increased cytoplasmic TDP-43 reduces global protein synthesis by interacting with RACK1 on
1571 polyribosomes. Human molecular genetics. 2017;26(8):1407-18.
1572 48. Bjork RT, Mortimore NP, Loganathan S, Zarnescu DC. Dysregulation of Translation in
1573 TDP-43 Proteinopathies: Deficits in the RNA Supply Chain and Local Protein Production. Front
1574 Neurosci. 2022;16:840357.
1575 49. Piol D, Robberechts T, Da Cruz S. Lost in local translation: TDP-43 and FUS in
1576 axonal/neuromuscular junction maintenance and dysregulation in amyotrophic lateral sclerosis.
1577 Neuron. 2023;111(9):1355-80.

1578 50. Zhong J, Gunner G, Henninger N, Schafer DP, Bosco DA. Intravital Imaging of
1579 Fluorescent Protein Expression in Mice with a Closed-Skull Traumatic Brain Injury and Cranial
1580 Window Using a Two-Photon Microscope. J Vis Exp. 2023(194).
1581 51. Dogan EO, Bouley J, Zhong J, Harkins AL, Keeler AM, Bosco DA, et al. Genetic ablation
1582 of Sarm1 attenuates expression and mislocalization of phosphorylated TDP-43 after mouse
1583 repetitive traumatic brain injury. Acta Neuropathol Commun. 2023;11(1):206.
1584 52. Flierl MA, Stahel PF, Beauchamp KM, Morgan SJ, Smith WR, Shohami E. Mouse closed
1585 head injury model induced by a weight-drop device. Nat Protoc. 2009;4(9):1328-37.
1586 53. Kim D, Paggi JM, Park C, Bennett C, Salzberg SL. Graph-based genome alignment and
1587 genotyping with HISAT2 and HISAT-genotype. Nat Biotechnol. 2019;37(8):907-15.
1588 54. Chen Y, Lun AT, Smyth GK. From reads to genes to pathways: differential expression
1589 analysis of RNA-Seq experiments using Rsubread and the edgeR quasi-likelihood pipeline.
1590 F1000Res. 2016;5:1438.
1591 55. Castanza AS, Recla JM, Eby D, Thorvaldsdottir H, Bult CJ, Mesirov JP. Extending
1592 support for mouse data in the Molecular Signatures Database (MSigDB). Nat Methods.
1593 2023;20(11):1619-20.
1594 56. Liberzon A, Birger C, Thorvaldsdottir H, Ghandi M, Mesirov JP, Tamayo P. The
1595 Molecular Signatures Database (MSigDB) hallmark gene set collection. Cell Syst.
1596 2015;1(6):417-25.
1597 57. Liberzon A, Subramanian A, Pinchback R, Thorvaldsdottir H, Tamayo P, Mesirov JP.
1598 Molecular signatures database (MSigDB) 3.0. Bioinformatics. 2011;27(12):1739-40.
1599 58. Mootha VK, Lindgren CM, Eriksson KF, Subramanian A, Sihag S, Lehar J, et al. PGC-
1600 1alpha-responsive genes involved in oxidative phosphorylation are coordinately downregulated
1601 in human diabetes. Nat Genet. 2003;34(3):267-73.
1602 59. Subramanian A, Tamayo P, Mootha VK, Mukherjee S, Ebert BL, Gillette MA, et al. Gene
1603 set enrichment analysis: a knowledge-based approach for interpreting genome-wide expression
1604 profiles. Proc Natl Acad Sci U S A. 2005;102(43):15545-50.
1605 60. Funes S, Jung J, Gadd DH, Mosqueda M, Zhong J, Shankaracharya, et al. Expression
1606 of ALS-PFN1 impairs vesicular degradation in iPSC-derived microglia. Nat Commun.
1607 2024;15(1):2497.
1608 61. Tyanova S, Temu T, Cox J. The MaxQuant computational platform for mass
1609 spectrometry-based shotgun proteomics. Nat Protoc. 2016;11(12):2301-19.
1610 62. Tyanova S, Temu T, Sinitcyn P, Carlson A, Hein MY, Geiger T, et al. The Perseus
1611 computational platform for comprehensive analysis of (prote)omics data. Nat Methods.
1612 2016;13(9):731-40.
1613 63. Schindelin J, Arganda-Carreras I, Frise E, Kaynig V, Longair M, Pietzsch T, et al. Fiji: an
1614 open-source platform for biological-image analysis. Nat Methods. 2012;9(7):676-82.
1615 64. Kamentsky L, Jones TR, Fraser A, Bray MA, Logan DJ, Madden KL, et al. Improved
1616 structure, function and compatibility for CellProfiler: modular high-throughput image analysis
1617 software. Bioinformatics. 2011;27(8):1179-80.
1618 65. Jumper J, Evans R, Pritzel A, Green T, Figurnov M, Ronneberger O, et al. Highly
1619 accurate protein structure prediction with AlphaFold. Nature. 2021;596(7873):583-9.
1620 66. Darnell JC, Van Driesche SJ, Zhang C, Hung KY, Mele A, Fraser CE, et al. FMRP stalls
1621 ribosomal translocation on mRNAs linked to synaptic function and autism. Cell.
1622 2011;146(2):247-61.
1623 67. Dogan EO, Simonini SR, Bouley J, Weiss A, Brown RH, Jr., Henninger N. Genetic
1624 Ablation of Sarm1 Mitigates Disease Acceleration after Traumatic Brain Injury in the
1625 SOD1(G93A) Transgenic Mouse Model of Amyotrophic Lateral Sclerosis. Ann Neurol. 2025.
1626 68. Curzon P, Rustay NR, Browman KE. Cued and Contextual Fear Conditioning for
1627 Rodents. 2nd ed: CRC Press/Taylor & Francis, Boca Raton (FL); 2009 2009.

1628 69. Maren S, Quirk GJ. Neuronal signalling of fear memory. Nat Rev Neurosci.
1629 2004;5(11):844-52.
1630 70. Querfurth H, Lee HK. Mammalian/mechanistic target of rapamycin (mTOR) complexes in
1631 neurodegeneration. Mol Neurodegener. 2021;16(1):44.
1632 71. Simon DW, McGeachy MJ, Bayir H, Clark RS, Loane DJ, Kochanek PM. The far-
1633 reaching scope of neuroinflammation after traumatic brain injury. Nat Rev Neurol.
1634 2017;13(3):171-91.
1635 72. Hubbard WB, Joseph B, Spry M, Vekaria HJ, Saatman KE, Sullivan PG. Acute
1636 Mitochondrial Impairment Underlies Prolonged Cellular Dysfunction after Repeated Mild
1637 Traumatic Brain Injuries. J Neurotrauma. 2019;36(8):1252-63.
1638 73. Wang W, Wang L, Lu J, Siedlak SL, Fujioka H, Liang J, et al. The inhibition of TDP-43
1639 mitochondrial localization blocks its neuronal toxicity. Nat Med. 2016;22(8):869-78.
1640 74. Yoshida H, Matsui T, Yamamoto A, Okada T, Mori K. XBP1 mRNA is induced by ATF6
1641 and spliced by IRE1 in response to ER stress to produce a highly active transcription factor.
1642 Cell. 2001;107(7):881-91.
1643 75. Hasan R, Humphrey J, Bettencourt C, Newcombe J, Consortium NA, Lashley T, et al.
1644 Transcriptomic analysis of frontotemporal lobar degeneration with TDP-43 pathology reveals
1645 cellular alterations across multiple brain regions. Acta Neuropathol. 2022;143(3):383-401.
1646 76. Pineda SS, Lee H, Ulloa-Navas MJ, Linville RM, Garcia FJ, Galani K, et al. Single-cell
1647 dissection of the human motor and prefrontal cortices in ALS and FTLD. Cell.
1648 2024;187(8):1971-89 e16.
1649 77. Perucho L, Artero-Castro A, Guerrero S, Ramon y Cajal S, ME LL, Wang ZQ. RPLP1, a
1650 crucial ribosomal protein for embryonic development of the nervous system. PLoS One.
1651 2014;9(6):e99956.
1652 78. Moisse K, Volkening K, Leystra-Lantz C, Welch I, Hill T, Strong MJ. Divergent patterns
1653 of cytosolic TDP-43 and neuronal progranulin expression following axotomy: implications for
1654 TDP-43 in the physiological response to neuronal injury. Brain Res. 2009;1249:202-11.
1655 79. Mehta PR, Brown AL, Ward ME, Fratta P. The era of cryptic exons: implications for ALS-
1656 FTD. Mol Neurodegener. 2023;18(1):16.
1657 80. Rouaux C, Gonzalez De Aguilar JL, Dupuis L. Unmasking the skiptic task of TDP-43.
1658 EMBO J. 2018;37(11).
1659 81. Arnold ES, Ling SC, Huelga SC, Lagier-Tourenne C, Polymenidou M, Ditsworth D, et al.
1660 ALS-linked TDP-43 mutations produce aberrant RNA splicing and adult-onset motor neuron
1661 disease without aggregation or loss of nuclear TDP-43. Proc Natl Acad Sci U S A.
1662 2013;110(8):E736-45.
1663 82. Fratta P, Sivakumar P, Humphrey J, Lo K, Ricketts T, Oliveira H, et al. Mice with
1664 endogenous TDP-43 mutations exhibit gain of splicing function and characteristics of
1665 amyotrophic lateral sclerosis. EMBO J. 2018;37(11).
1666 83. Polymenidou M, Lagier-Tourenne C, Hutt KR, Huelga SC, Moran J, Liang TY, et al. Long
1667 pre-mRNA depletion and RNA missplicing contribute to neuronal vulnerability from loss of TDP-
1668 43. Nat Neurosci. 2011;14(4):459-68.
1669 84. Yang C, Qiao T, Yu J, Wang H, Guo Y, Salameh J, et al. Low-level overexpression of
1670 wild type TDP-43 causes late-onset, progressive neurodegeneration and paralysis in mice.
1671 PLoS One. 2022;17(2):e0255710.
1672 85. Chu BW, Kovary KM, Guillaume J, Chen LC, Teruel MN, Wandless TJ. The E3 ubiquitin
1673 ligase UBE3C enhances proteasome processivity by ubiquitinating partially proteolyzed
1674 substrates. J Biol Chem. 2013;288(48):34575-87.
1675 86. Gaetani M, Zubarev RA. Proteome Integral Solubility Alteration (PISA) for High-
1676 Throughput Ligand Target Deconvolution with Increased Statistical Significance and Reduced
1677 Sample Amount. Methods Mol Biol. 2023;2554:91-106.

1678 87. Li J, Van Vranken JG, Paulo JA, Huttlin EL, Gygi SP. Selection of Heating Temperatures
1679 Improves the Sensitivity of the Proteome Integral Solubility Alteration Assay. J Proteome Res.
1680 2020;19(5):2159-66.
1681 88. Savitski MM, Reinhard FB, Franken H, Werner T, Savitski MF, Eberhard D, et al.
1682 Tracking cancer drugs in living cells by thermal profiling of the proteome. Science.
1683 2014;346(6205):1255784.
1684 89. Brohee S, van Helden J. Evaluation of clustering algorithms for protein-protein
1685 interaction networks. BMC Bioinformatics. 2006;7:488.
1686 90. Szklarczyk D, Kirsch R, Koutrouli M, Nastou K, Mehryary F, Hachilif R, et al. The
1687 STRING database in 2023: protein-protein association networks and functional enrichment
1688 analyses for any sequenced genome of interest. Nucleic Acids Res. 2023;51(D1):D638-D46.
1689 91. Cheng F, Chapman T, Venturato J, Davidson JM, Polido SA, Rosa-Fernandes L, et al.
1690 Proteomics Analysis of the TDP-43 Interactome in Cellular Models of ALS Pathogenesis. J
1691 Neurochem. 2025;169(5):e70079.
1692 92. Freibaum BD, Chitta RK, High AA, Taylor JP. Global analysis of TDP-43 interacting
1693 proteins reveals strong association with RNA splicing and translation machinery. J Proteome
1694 Res. 2010;9(2):1104-20.
1695 93. Zeng C, Han S, Pan Y, Huang Z, Zhang B, Zhang B. Revisiting the chaperonin T-
1696 complex protein-1 ring complex in human health and disease: A proteostasis modulator and
1697 beyond. Clin Transl Med. 2024;14(2):e1592.
1698 94. Luo J, Zhao H, Chen L, Liu M. Multifaceted functions of RPS27a: An unconventional
1699 ribosomal protein. J Cell Physiol. 2023;238(3):485-97.
1700 95. Lin Z, Kim E, Ahmed M, Han G, Simmons C, Redhead Y, et al. MRI-guided histology of
1701 TDP-43 knock-in mice implicates parvalbumin interneuron loss, impaired neurogenesis and
1702 aberrant neurodevelopment in amyotrophic lateral sclerosis-frontotemporal dementia. Brain
1703 Commun. 2021;3(2):fcab114.
1704 96. Kelmer Sacramento E, Kirkpatrick JM, Mazzetto M, Baumgart M, Bartolome A, Di Sanzo
1705 S, et al. Reduced proteasome activity in the aging brain results in ribosome stoichiometry loss
1706 and aggregation. Mol Syst Biol. 2020;16(6):e9596.
1707 97. Amirbeigiarab S, Kiani P, Velazquez Sanchez A, Krisp C, Kazantsev A, Fester L, et al.
1708 Invariable stoichiometry of ribosomal proteins in mouse brain tissues with aging. Proc Natl Acad
1709 Sci U S A. 2019;116(45):22567-72.
1710 98. Zhao B, Cowan CM, Coutts JA, Christy DD, Saraph A, Hsueh SCC, et al. Targeting
1711 RACK1 to alleviate TDP-43 and FUS proteinopathy-mediated suppression of protein translation
1712 and neurodegeneration. Acta Neuropathol Commun. 2023;11(1):200.
1713 99. Bhavsar RB, Makley LN, Tsonis PA. The other lives of ribosomal proteins. Hum
1714 Genomics. 2010;4(5):327-44.
1715 100. Simsek D, Barna M. An emerging role for the ribosome as a nexus for post-translational
1716 modifications. Curr Opin Cell Biol. 2017;45:92-101.
1717 101. Ali A, Garde R, Schaffer OC, Bard JAM, Husain K, Kik SK, et al. Adaptive preservation
1718 of orphan ribosomal proteins in chaperone-dispersed condensates. Nat Cell Biol.
1719 2023;25(11):1691-703.
1720 102. Nagano S, Jinno J, Abdelhamid RF, Jin Y, Shibata M, Watanabe S, et al. TDP-43
1721 transports ribosomal protein mRNA to regulate axonal local translation in neuronal axons. Acta
1722 Neuropathol. 2020;140(5):695-713.
1723 103. Tank EM, Figueroa-Romero C, Hinder LM, Bedi K, Archbold HC, Li X, et al. Abnormal
1724 RNA stability in amyotrophic lateral sclerosis. Nat Commun. 2018;9(1):2845.
1725 104. Chou A, Krukowski K, Jopson T, Zhu PJ, Costa-Mattioli M, Walter P, et al. Inhibition of
1726 the integrated stress response reverses cognitive deficits after traumatic brain injury. Proc Natl
1727 Acad Sci U S A. 2017;114(31):E6420-E6.

1728 105. Huang WP, Ellis BCS, Hodgson RE, Sanchez Avila A, Kumar V, Rayment J, et al.
1729 Stress-induced TDP-43 nuclear condensation causes splicing loss of function and STMN2
1730 depletion. Cell Rep. 2024;43(7):114421.
1731 106. Rifai OM, Waldron FM, O'Shaughnessy J, Read FL, Gilodi M, Pastore A, et al. Amygdala
1732 TDP-43 pathology is associated with behavioural dysfunction and ferritin accumulation in
1733 amyotrophic lateral sclerosis. bioRxiv. 2024.
1734 107. Wilkins OG, Chien M, Wlaschin JJ, Barattucci S, Harley P, Mattedi F, et al. Creation of
1735 de novo cryptic splicing for ALS and FTD precision medicine. Science. 2024;386(6717):61-9.
1736 108. Francois-Moutal L, Perez-Miller S, Scott DD, Miranda VG, Mollasalehi N, Khanna M.
1737 Structural Insights Into TDP-43 and Effects of Post-translational Modifications. Front Mol
1738 Neurosci. 2019;12:301.
1739 109. Shenouda M, Xiao S, MacNair L, Lau A, Robertson J. A C-Terminally Truncated TDP-43
1740 Splice Isoform Exhibits Neuronal Specific Cytoplasmic Aggregation and Contributes to TDP-43
1741 Pathology in ALS. Front Neurosci. 2022;16:868556.
1742 110. Elliott E, Bailey O, Waldron FM, Hardingham GE, Chandran S, Gregory JM. Therapeutic
1743 Targeting of Proteostasis in Amyotrophic Lateral Sclerosis-a Systematic Review and Meta-
1744 Analysis of Preclinical Research. Front Neurosci. 2020;14:511.
1745